Mössbauer Effect Reference and Data Journal

April • Volume 48 • Number 02

Development of Fe^{II} Tetranuclear Cages: Spin Crossover and Their Ammonia Sensing Application

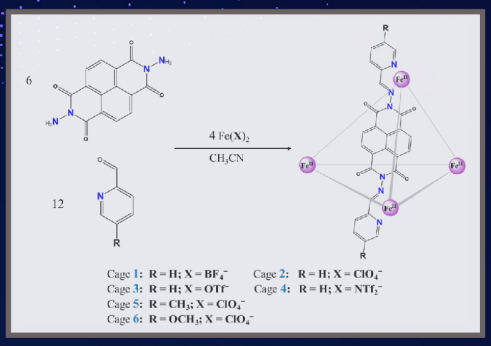

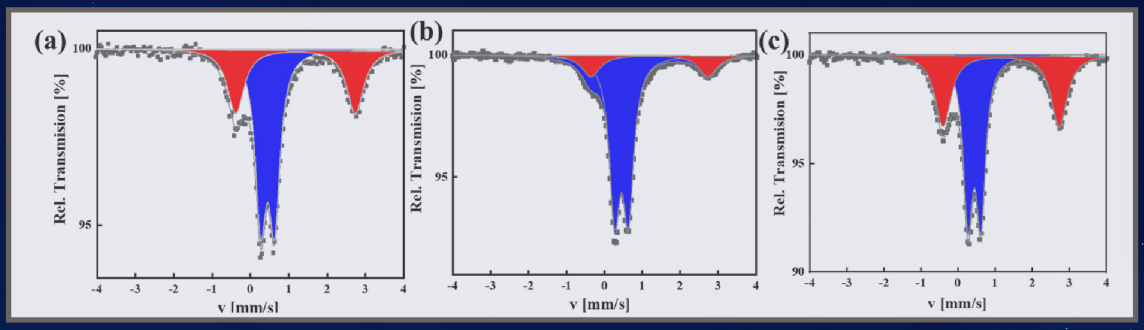

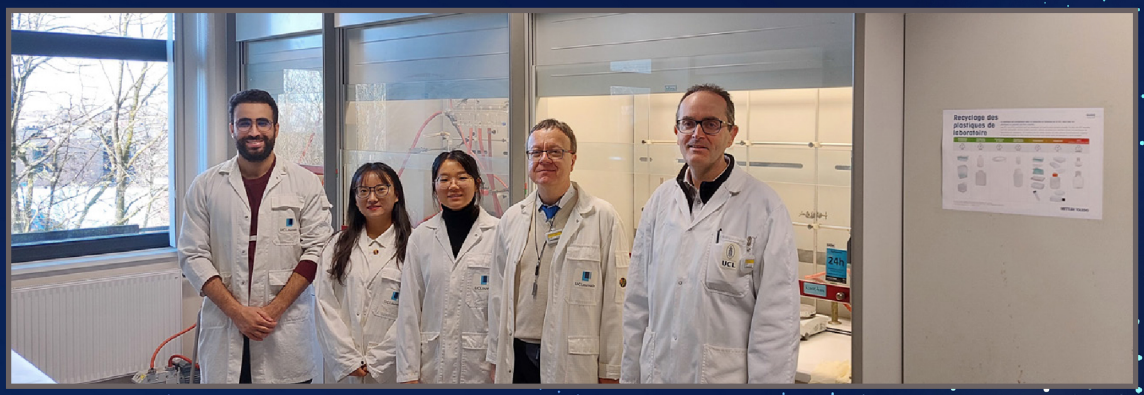

Mössbauer Effect Reference and Data Journal

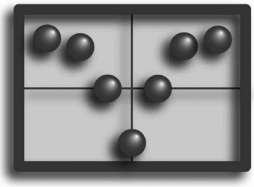

The *Mössbauer Effect Reference and Data Journal (MERDJ)* is published ten times a year (each month excluding January and February) plus an Index Issue at the end of December by the Mössbauer Effect Data Center.

Subscriptions: The annual subscription rate for Volume 48 (2025) is US$1,500.00 ($1,200.00 without the Index Issue). Subscription inquiries and address changes should be addressed to the General Manager at the address below.

Mössbauer Effect Data Center
Dalian Institute of Chemical Physics
Chinese Academy of Sciences
457 Zhongshan Road, Dalian
116023, China

Tel: +86 411 8437 9407
Email: medc@dicp.ac.cn
Web: www.medc.dicp.ac.cn

ISSN 0163-9587

On the cover:
This issue our front cover is focusing on the pictures from Prof. Yann Garcia's group at UCLouvain in Belgium. We highlight the work of a young Mössbauer spectroscopist, Dr. **Weiyang Li** and the interview with Prof. **Tadeusz Szumiata**. (See more in Editor's Comments and in the enclosed Mössbauer Spectroscopy Newsletter.)

Mössbauer Effect Reference and Data Journal

April 2025 • Volume 48 • Number 2

Contents

Contents....29
Reference Listing....31
Data Listing....36
Subject Index....45
Abbreviation Listing....46
Isotope Index....46
Mössbauer Newsletter....47

Editor's Comments

Development of Fe(II) Tetranuclear Cages: Spin Crossover and Their Ammonia Sensing Application

This month, we highlight the work of a young Mössbauer spectroscopist, **Weiyang Li**, who was awarded a PhD degree in coordination chemistry and material science from Université catholique de Louvain (UCLouvain) at the end of 2023. Dr Li recently presented an e-oral contribution titled 'Spin state versatility in $Fe(II)_4L_6$ supramolecular cages with a pyridyl-hydrazone ligand scaffold modulated by solvents and counter anions' at the ESR & Rising star e-symposium held on the occasion of the GFSM 2025 international conference organized at the end of April 2025 in Louvain-la-Neuve, Belgium.

Several participants asked for the definition of ESR. ESR is an acronym which stands for 'Early Stage Researcher'. According to the EU community, ESRs shall, at the time of recruitment by their host organization, be in the first four years (full-time equivalent research experience) of their research careers and have not been awarded a doctoral degree. These scientists form the next generation of spectroscopists who are expected to animate and enrich the future of our community. Knowing better their work will allow not only allow them to establish networking contacts but also generate future opportunities and stimulate new research ideas and concepts.

Dr. **Weiyang Li**, who was educated in China and in Belgium (Louvain-la-Neuve), returned to his home country to take an assistant professor position at the Liaoning Petrochemical University which was founded in 1950 in Dalian, China.

We wish him much success!

Yann Garcia
Associate Editor
Institute of Condensed Matter and Nanosciences
Université Catholique de Louvain, Belgium

Mössbauer Effect Data Center

is pleased to offer these publications and services to the international Mössbauer community...

Mössbauer Effect Reference and Data Journal

The *Journal* reports as thoroughly as possible all published information on Mössbauer spectroscopy. An annual subscription includes ten issues plus an index issue. Each issue includes a Reference Listing, a Data Listing, an Isotope Index, a Subject Index, and the *Mössbauer Spectroscopy Newsletter*.

Mössbauer Web Sites
ON THE WORLD WIDE WEB

The Mössbauer Effect Data Center developed and administers two separate Web sites for the Mössbauer community (<www.moss.dicp.ac.cn> and <www.medc.dicp.ac.cn>). These sites provide Mössbauer researchers with pertinent and timely information, free of charge. Included on the sites are general information pertinent to the Mössbauer community, news items, regional lab information, position postings, information on upcoming conferences, the most recent *Mössbauer Spectroscopy Newsletter*, IBAME information, an E-Mail and Fax Directory of Mössbauer Authors, links to Mössbauer instrument and source suppliers, and further information regarding the Center's products and services. Access to the MEDC Web-Access Database is also provided through the MEDC site. Researchers may now access and search the MEDC database *from their computers* via the MEDC Web site.

For further information about these and our many other publications and services for the Mössbauer community, please visit us at our Web site

Dalian Institute of Chemical Physics
Chinese Academy of Sciences
457 Zhongshan Road, Dalian 116023, China
Phone: +86-411-84379159
Fax: +86-411-84685940
Email: medc@dicp.ac.cn
Web: www.medc.dicp.ac.cn www.moss.dicp.ac.cn

Code	Reference
20S095	H.Suzuki, *Intermetallics* **119**,106713/1-8(2020) Structural analysis and magnetic properties of lattice distortions from hexagonal to tetragonal systems in non-equilibrium Y-Fe alloys.
20V020	A.V. N., P.K.Rastogi, T.S., V.S., S.Shaji, R.R.Varimalla, M.A.Garza-Navarro, S.Thomas, T.N.Narayanan*, and M.R.Anantharaman*, *Sustainable Energy Fuels* **4**(8),3915-25(2020) Engineering nanostructured spinel ferrites by co-substitution for total water electrolysis by preferential exposure of metal cations on the surface.
21A044	B.Assi, Z.Bitar*, W.Malaeb, R.Sayed Hassan, N.Yaacoub, and R.Awad, *Phys. Scr.* **96**(8),085803/1-12(2021) Investigating the role of diamagnetic Cd^{2+} ions on the structural, optical, and magnetic properties of YIG.
21H029	C.X.Hu, H.H.Jin, B.S.Liu, L.H.Liang, Z.Wang, D.Chen, D.P.He*, and S.C.Mu*, *Nano Energy* **82**,105714/1-9(2021) Propagating Fe-N_4 active sites with Vitamin C to efficiently drive oxygen electrocatalysis.
24E008	N.V.Ershov, N.M.Kleinerman, V.A.Lukshina, and A.V.Timofeeva, *Phys. Met. Metallogr.* **125**(12),1399-407(2024) Distribution of magnetization in single-crystals of iron-silicon soft magnetic alloys before and after heat treatments.
24E009	A.V.Egorysheva, E. F.Popova, O.G.Ellert, E.V.Khramov, S.Y.Kottsov, and E.S.Kulikova, *Russ. J. Inorg. Chem.* **69**(14),1995-2002(2024) Structural features of Mg-containing solid solutions based on Y_2FeTaO_7.
24F018	H.Z.Fei, Y.F.Lyu, F.Wang, C.A.McCammon, and T.Katsura, *Earth Planet. Sci. Lett.* **646**,118983/1-12(2024) The effects of trivalent cations (Al and Fe) on the grain growth rates of bridgmanite.
24F019	M.S.Fataftah, D.W.N.Wilson, Z.Mathe, T.J.Gerard, B.Q.Mercado, S.DeBeer*, and P.L.Holland*, *ACS Cent. Sci.* **10**(10),1910-9(2024) Inserting three-coordinate nickel into [4Fe-4S] clusters.
24O011	M.Ochmann, L.Machala*, M.Maslan, V.Heger, and T.Kratky, *Materials* **17**(4),857/1-15(2024) Zinc ferrite nanoparticle coatings on austenitic alloy steel.
24S081	K.D.Spielvogel, E.J.Campbell, S.R.Chowdhury, F.Benner, S.Demir, G.P.Hatzis, H.R.Petras, D.Sembukuttiarachchige, J.J.Shepherd, C.M.Thomas, B.Vlaisavljevich, and S.R.Daly*, *Chem. Commun. (Cambridge, U. K.)* **60**(64),8399-402(2024) Modulation of Fe-Fe distance and spin in diiron complexes using tetradentate ligands with different flanking donors.
24S082	Y.S.Soboleva, S.Sandalova, A.V.Sobolev, and I.A.Presnyakov, *Inorg. Mater.* **60**(10),1226-30(2024) Probe Mössbauer study of magnetically ordered manganite $ScMn_{570.996}Fe_{0.004}O_3$.
24Z033	B.F.Zhang, J.P.Joyce, N.J.Wolford, W.W.Brennessel, S.DeBeer, and M.L.Neidig*, *Angew. Chem., Int. Ed.* **63**(36), e202405113/1-6(2024) Unusual S=1 four-coordinate Fe(IV) complexes supported by bisamide ligands: syntheses, characterization, and electronic structures.
25A004	N.A.Algarou, R.K.Aldakheel, M.A.Almessiere*, A.Baykal*, H.Güngunes, S.Caliskan, and A.Mihmanlı, *Inorg. Chem. Commun.* **175**,114103/1-10(2025) Tunned the structure and magnetic characteristics of noble metal (Pd)-doped Ba-Sr nanohexaferrites.
25A005	L.H.F.Andrade, L.M.B.Campos, T.A.Pedrosa, A.Krohling, J.D.Ardisson, and L.E.Fernandez-Outon*, *AIP Adv.* **15**(3),035105/1-6(2025) Magnetic properties and structural characterization of $Co_xFe_{(1-x)}Al$ Heusler alloys synthesized from Co/FeAl multilayers.
25A006	Y.V.Alca-Ramos, N.R.Checca-Huaman, R.Rueda-Vellasmin, E.C.Passamani, and J.A.Ramos-Guivar*, *Nanomaterials* **15**(5),382/1-25(2025) Biosynthesis scale-up process for magnetic iron-oxide nanoparticles using eucalyptus globulus extract and their separation properties in lubricant-water emulsions.
25A007	B.Ali, J.L.Huang, J.Zhang, S.L.Sun*, and Y.Zhang*, *Catal. Sci. Technol.* **15**(7),2160-74(2025) Iron foam catalysts for forming olefins via Fischer-Tropsch synthesis.
25B005	L.Bereczki, KA.Beres, E.Kováts, A.Benyei, R.Hühn, D.M.Melgalvis, Z.Homonnay, L.Kótai, P.Bombicz, and T.Rekis*, *Cryst. Growth Des.* **25**(4),1148-54(2025) Incommensurate displacive and occupational modulation in hexakis(urea-O)iron(III) nitrate.
25B006	V.Bilovol, P.Jelen, K.Mech, K.Sokolowski, P.Botella, E.Bandiello, F.J.Manjon, and D.Errandonea, *J. Solid State Chem.* **347**,125338/1-10(2025) Effect of sintering temperature on cation distribution in $CoFe_2O_4$ nanoparticles.
25B007	A.Bajorek, B.Liszka, B.Szostak, M.Dulski, M.Pawlyta, and J.M.Grenèche, *Mater. Sci. Eng., B* **313**,117942/1-20(2025) Exploring the interplay between structure, microstructure and magnetism induced by multi-step calcination in spinel ferrite-based NZFO/f-MWCNTs nanocomposites with 2 weight% of NZFO towards possible applications.
25B008	W.R.Berg, M.Reimann, R.Sievers, S.M.Rupf, J.Schlögl, K.Weißer, K.B.Krause, C.Limberg, M.Kaupp, and M.Malischewski*, *J. Am. Chem. Soc.* **147**(4),3039-46(2025) Solvent-dependent reactivity of $Fe(CO)_5$ under superacidic and oxidative conditions.

Code	Reference
25C005	S.Caspani, F.J.Fernandez-Alonso, S.M.Gonçalves, C.Martín-Morales, B.Cortes-Llanos, B.J.C.Vieira, J.C.B.Waerenborgh, L.C.J.Pereira, A.Apolinario, J.P.Araújo, M.V.Gómez-Gaviro, V.Torres-Costa, M.J.Manso Silvan, and C.T.de Sousa*, *ACS Appl. Mater. Interfaces* **17**(11),16602-15(2025) Anisotropic porous iron-based nanoparticles through two-step hydrothermal and hydrogen-based reduction: enhanced magnetic performance for potential biomedical applications.
25C006	Y.Chen, Y.Y.Quan, Y.P.Liu, M.Yuan, J.Q.Wang, C.Chen, C.Q.Huang*, X.Y.Fang, J.Zhang, X.H.Feng, W.F.Tan, J.S.Li, and H.Yin*, *Environ. Pollut. (Oxford, U. K.)* **367**,125593/1-10(2025) Effects of dimethylarsenate coprecipitation with ferrihydrite on Fe(II)-induced mineral transformation and the release of dimethylarsenate.
25C007	J.Cong, S.H.Luo*, Q.Sun, X.Liu, Y.K.Wang, S.X.Yan, and P.W.Li, *Sep. Purif. Technol.* **363**(Part_3), 132326/1-14(2025) Study on deep synergistic leaching mechanism of spent lithium iron phosphate under the H_2SO_4-H_2O_2 system and precise chemical precipitation recovery strategy of lithium carbonate.
25C008	W.X.Chen, H.Y.Zhu, F.Liu, X.Zeng, Y.J.Mao, and A.J.Yang*, *Constr. Build. Mater.* **471**,140595/1-12(2025) Green transformation of mining waste: synergistic effects of coal mine drainage sludge and industrial by-products in high-performance geopolymer production and environmental benefits.
25D003	V.Duran-Egido, J.P.Darby, M.J.Cliffe, J.S.Garitaonandia, P.Grande-Fernandez, A.J.Morris, J.Carretero-Gonzalez*, and E.Castillo-Martínez*, *Angew. Chem., Int. Ed.* **64**(14),e202424416/1-14(2025) Easily water-synthesisable iron-chloranilate frameworks as high energy and high-power cathodes for sustainable alkali-ion batteries.
25D004	K.Dadwal, M.Fabian, I.Tolnai, S.Sharma, R.Kaur, M.Gracheva, K.Kovacs, Z.Klencsár, and A.Khanna*, *RSC Adv.* **15**(7),5286-304(2025) Neutron, X-ray diffraction, DSC, Raman, Mössbauer and leaching studies of iron phosphate glasses and crystalline phases.
25E002	R.E.El Shater, A.W.Awad, H.H.El-Bahnasawy, T.M.Meaz, and E.H.El-Ghazzawy*, *Mater. Sci. Semicond. Process.* **192**,109451/1-22(2025) Comprehensive analysis of the synthesis and characterizations of Cr-substituted Cd-Cu ferrite: insights from Mössbauer and impedance spectroscopy.
25E003	J.S.Evarts, B.J.Riley*, C.E.Lonergan, M.S.Harris, J.C.Bai, E.W.Bohannan, I.Ajoku, S.Chong, and J.S.McCloy, *ACS Sustainable Resour. Manage.* **2**(3),514-23(2025) Synergy in materials: leveraging phosphosilicate waste forms for electrochemical salt waste.
25F001	K.M.Fugami, G.S.Black, T.Kowalczyk, T.Seda, and J.D.Gilbertson*, *J. Am. Chem. Soc.* **147**(9),7274-81(2025) Intermolecular N-N coupling of a dinitrosyl iron complex induced by hydrogen bond donors in the secondary coordination sphere.
25F002	E.Fanesi, D.Di Genova*, P.Valdivia, D.Bondar, S.Dominijanni, S.Abeykoon, G.Giuliani, A.Kurnosov, G.Giordano, M.Cassetta, A.Vona, C.Romano, and F.Arzilli, *J. Volcanol. Geotherm. Res.* **461**,108276/1-19(2025) A review of the differential scanning calorimetry shift-factor approach: application to Colli Albani melt viscosity and implications for mafic Plinian eruptions.
25F003	K.V.Frolov, E.S.Smirnova, E.V.Sidorova, O.A.Alekseeva, and I.A.Gudim, *JETP Lett.* **121**(2),132-41(2025) ^{57}Fe Mössbauer spectroscopy study of $SmFe_{3-x}Al_x(BO_3)_4$ (x=0-0.28) multiferroics.
25F004	D.I.Fazlizhanova, P.A.Sinitsyn, F.G.Vagizov, R.G.Batulin, A.L.Zinnatullin, and R.M.Eremina, *J. Supercond. Novel Magn.* **38**(2),104/1-11(2025) Magnetic properties of the composite formed from $LaSr(CoFe)_{1/2}O_4$ ruddlesden-popper phase and $(LaSr)_{1/2}(CoFe)_{1/2}O_3$ perovskite.
25G006	L.P.Griffin, A.K.Bauer, A.E.Crumpton, M.A.Ellwanger, A.Heilmann, A.Wiesner, M.L.Neidig, and S.Aldridge*, *Chem. - Eur. J.* **31**(18),e202404451/1-10(2025) Synthesis, and structural and spectroscopic analysis of trielyl-derived complexes of iron.
25G007	S.L.C.Gonzales, A.M.M.Navarro, D.Errandonea, V.Bilovol, and L.A.Errico*, *Interactions (Cham, Switz.)* **246**(1), 57/1-13(2025) DFT study of structural, electronic and hyperfine properties of $Ge_{16}Sb_8Te_{28}$ and $Ge_{12}Sb_8Sn_4Te_{28}$ alloys for thermoelectric applications.
25G008	D.Garzon, C.Ostos, L.C.Sanchez, J.M.Marin Ramirez, and O.Arnache, *Metall. Mater. Trans. A* **56**(4), 1205-15 (2025) Evidence of magnetocaloric effect in $(Fe_{63}Ni_{37})_{89}B_{11}$ nanostructured magnetic alloys.
25H005	J.Herrera, K.E.García, V.Perez, J.F.Marco*, and C.A.Barrero Meneses*, *ACS OMEGA* **10**(12),11770-85(2025) Distinct physical properties of β-hematin in two synthetic media: compelling evidence.
25H006	P.Hewitt, M.P.Hendrich, and S.J.Elliott*, *Chem. Sci.* **16**(14),6070-8(2025) Reactivity of canonical bacterial cytochrome C peroxidases: insights into the electronic structure of compound I.
25H007	J.Hassen, and J.Silver, *Chimia* **79**(1-2),84-92(2025) Mössbauer spectroscopy as a valuable analysis technique in biomedical research.
25H008	T.X.Huang, Z.B.Song, A.Jain, and Y.G.Wang*, *J. Mater. Sci.: Mater. Electron.* **36**(10),586/1-12(2025) Role of Cu

Code	Reference
	in tailoring the structure and soft magnetic performance of Fe-based nanocrystalline alloys during two-step annealing.
25H009	T.X.Huang, Q.Yan, F.G.Chen, A.Jain, H.Z.Zhou, and Y.G.Wang*, *J. Magn. Magn. Mater.* **623**,173005/1-7(2025) Reducing the annealing heating rate sensitivity of $Fe_{83.5}Si_3B_{10}P_2Cu_{1.5}$ soft magnetic nanocrystalline alloy by adjusting the B/P ratio.
25J003	J.T.Janetzki, D.S.Brown, F.Daumann, I.H.Ismail, R.W.Gable, M.A.Hay, R.J.Mulder, A.A.Starikova, B.Weber, M.J.Giansiracusa, and C.Boskovic*, *Chem. Sci.* **16**(14),5857-71(2025) Thermal- and light-induced valence tautomerism with a concerted spin transition in an iron tris(diimine) complex.
25J004	R.Jayashire, M.M.Raja, V.R.Reddy, A.Lakhani, and K.Ravichandran*, *J. Alloys Compd.* **1020**,179228/1-11(2025) Effect of annealing on the structure, magnetic and electrical properties of bulk $Fe_2Cr_{1-x}Co_xSi$ heusler alloys.
25K010	M.Kassem, C.J.Benmore, A.Tverjanovich, M.Bokova, M.Khomenko, T.Usuki, A.Sokolov, D.Fontanari, S.Bereznev, K.Ohara, M.Fourmentin, P.Masselin, and E.Bychkov*, *ACS Appl. Mater. Interfaces* **17**(11), 17075-95(2025) Atomic structure, dynamics, changes in chemical bonding and semiconductor-metal transition in Sb_2Se_3: a remarkable material for quantum networks and energy applications.
25K011	V.Kumar, A.C.Ghosh, Y.Draoui, M.M.Wang, K.van Hecke, A.Rotaru, and Y.Garcia*, *Eur. J. Inorg. Chem.* **28**(7), e202400753/1-6(2025) Thermally induced Fe^{II} spin crossover hybrid complex incorporating para-sulfocinnamic acid.
25K012	H.I.Kim, I.Moon*, M.Kim, H.J.Lee, H.Choi, Y.R.Uhm, L.Liu, J.Kim, and W.Kim, *Plos one* **20**(1),e0316540/ 1-22(2025) Characterization and quantification of iron species in the banded iron formations (BIFs) in China Craton to explore the potential for H_2 production using XRD and Mössbauer spectroscopy.
25K013	M.Kasprzyk, G.Opila, A.Hinz, S.Stankiewicz, M.Bzowska, K.Wolski, J.Dulinska-Litewka, J.Przewoznik, C.Kapusta, and A.Karewicz*, *ACS Appl. Mater. Interfaces* **17**(6),9059-73(2025) Hyaluronic acid-coated SPIONs with attached folic acid as potential T2 MRI contrasts for anticancer therapies.
25K014	D.V.Karpov, S.A.Vorobyev, O.A.Bayukov, Y.V.Knyazev, D.A.Velikanov, S.M.Zharkov, Y.V.Larichev, S.V.Saikova, D.Zitoun, and YL.Mikhlin*, *J. Am. Chem. Soc.* **147**(10),8467-77(2025) Unraveling the structure and properties of high-concentration aqueous iron oxide nanocolloids free of steric stabilizers.
25L006	Y.E.Li, J.Shine, C.Guguschev, M.Brützam, D.G.Schlom*, and N.Ravi, *AIP Adv.* **15**(1),015323/1-9(2025) Corroborating the magnetic easy axis of epitaxial (100) α-iron and (0001) $BaFe_{12}O_{19}$ thin films by ^{57}Fe Mössbauer spectroscopy.
25L007	Z.L.Li, Z.Y.Feng, M.Chen, Y.K.Song, Y.C.Dai, S.Mao, and H.Y.Zhao*, *Water Res.* **273**,122967/1-12(2025) Cathode-mediated electrochemical conversion of phenol to benzoquinone in wastewater: high yield rate and low energy consumption.
25L008	F.Y.Lai, L.Getzner, A.Rotaru, G.Molnar*, S.Cobo*, and A.Bousseksou*, *Chem. Mater.* **37**(2),636-43(2025) Drastic enhancement of electrical conductivity of metal-organic frameworks displaying spin crossover.
25L009	R.J.Li, R.J.Lewis*, A.Lopez-Martin, D.J.Morgan, T.E.Davies, D.Kordus, A.I.Dugulan, B.Roldan Cuenya, and G.J.Hutchings*, *Green Chem.* **27**(7),2065-77(2025) Promoting H_2O_2 direct synthesis through Fe incorporation into AuPd catalysts.
25M001	I.Mallek-Zouari, W.Ben Taazayet, J.M.Grenèche, L.Bessais, and N.Thabet Mliki, *Mater. Chem. Phys.* **332**, 130266/1-7(2025) Mössbauer spectrometry for investigating the magnetic properties of $Bi_2Fe_4O_9$ bismuth ferrite nanostructures.
25M002	M.Mauger, I.Makarchuk, Y.Molter, A.Sansone, F.Melin, P.Chaignon, P.Schaeffer, P.Adam, V.Schünemann, P.Hellwig, C.Ferreri, C.Chatgilialoglu, and M.Seemann*, *ChemBioChem* **26**(1),e202400844/1-10(2025) Towards bacterial resistance via the membrane strategy: enzymatic, biophysical and biomimetic studies of the lipid cis-trans isomerase of pseudomonas aeruginosa.
25M003	M.O.Moysa, A.V.Pavlenko, L.A.Shilkina, S.P.Kubrin, K.P.Andryushin, and L.A.Reznichenko, *Ceram. Int.* **51**(4), 5208-16(2025) Dielectric relaxation, crystal structure and magnetic phenomena in solid solutions based on alkali metal niobates and bismuth ferrite in a wide range of external influences.
25N001	L.Nodari, S.Conte*, L.Casini, M.Sisti, R.Fantini, A.F.Gualtieri, C.Molinari, C.Zanelli, D.Giordano, M.Dondi, and R.Arletti, *J. Eur. Ceram. Soc.* **45**(2),116947(2025) Role of iron-rich clays on sintering of porcelain stoneware tiles.
25N002	G.Niraula, J.A.H.Coaquira, E.O.P.Reyes, Y.Javed, E.Reguera, J.Garcia*, and S.K.Sharma*, *Results Chem.* **14**, 102066/1-9(2025) Hydrothermally synthesized Fe_3O_4 microparticles: structural, magnetic, Mössbauer and magneto-hyperthermia properties.
25N003	M.A.L.Nobre, F.R.Praxedes, U.F.Kaneko, F.F.Ivashita, A.Paesano Jr., and S.Lanfredi*, *J. Phys. Chem. Solids* **199**,

Code	Reference
	112578(2025) Analysis of the suppression of the ferroelectric-paraeletric transition and its Curie's temperature in a doped host-structure niobate.
25O001	J.Oh, S.L.Zheng, K.M.Carsch, T.P.Latendresse, C.E.Casaday, B.M.Campbell, and T.A.Betley*, *J. Am. Chem. Soc.* **147**(4),3174-84(2025) An open-shell Fe^{IV} nitrido.
25P001	O.Porodko, L.Kavan, M.Fabian*, B.Pitna Laskova, V.Sepelak, H.Kolev, K.L.da Silva, M.Lisnichuk, and M.Zukalova*, *Nanoscale* **17**(7),3739-51(2025) Preparation of novel lithiated high-entropy spinel-type oxyhalides and their electrochemical performance in Li-ion batteries.
25P002	PN.Phu, J.L.Lee*, S.Biswas, J.W.Ziller, EL.Bominaar, M.P.Hendrich, and A.S.Borovik*, *J. Am. Chem. Soc.* **147**(4), 3129-39(2025) Proton-induced switching of paramagnetism: reversible conversion between a low and high spin Co^{III} center within a heterobimetallic core.
25P003	G.Peters, D.Naidoo, R.M.Genga, D.Wamwangi, and O.Mouane, *Int. J. Refract. Met. Hard Mater.* **128**,107040/1-9(2025) Mössbauer characterisation and physical property measurements of Fe and FeNi bonded NbC cermets.
25P004	M.S.Pessoa, M.A.Sousa, P.S.Moscon, J. R. C.Proveti, L.C.Merino, P.C.Morais, F.Pelegrini, M.Parise, L.C.Figueiredo, and E.Baggio-Saitovitch, *Phys. B (Amsterdam, Neth.)* **697**,416736/1-6(2025) Unveiling unsaturated modes from multi-frequency ferromagnetic resonance using maghemite nanoparticles.
25R001	D.H.Ryan, *J. Supercond. Novel Magn.* **38**(1),5/1-5(2025) A ^{151}Eu Mössbauer investigation of magnetic ordering in the topological material candidate $EuZnBi_2$.
25R002	T.N.Rudneva, V. I.Korepanov, N.S.Ovanesyan, A.N.Utenyshev, P.V.Dorovatovskii, A.V.Kulikov, A.I.Dmitriev, M.V.Zhidkov, and M.G.Spirin, *J. Mol. Struct.* **1322**(Part_1),140311/1-10(2025) Neutral water-soluble μ-S nitrosyl iron complex with acetylcysteine non-silent in EPR spectra.
25R003	J.C.Rigby, J.Marcial, R.Pokorny, J.Klouzek, K.S.Han, N.M.Washton, P.Ferkl, P.Hrma, A.Scrimshire, P.A.Bingham, M.Hall, W.Eaton, and A.A.Kruger, *J. Am. Ceram. Soc.* **108**(2),e20192/1-12(2025) Boron nitride: novel ceramic reductant for low-activity waste vitrification.
25R004	D.Raenko, and A.L.Tchougreeff*, *J. Comput. Chem.* **46**(5),e27546/1-22(2025) Highly efficient numerical method for modeling mofs containing transition metal ions.
25S001	A.Sperling, M.P.Deutschmann, D.G.Ning*, J.Spielmann, T.Li, U.I.Kramm, H.Nirschl, B.Böhm, and A.Dreizler, *Fuel* **381**(Part_A),133147/1-9(2025) Oxidation progress and inner structure during single micron-sized iron particles combustion in a hot oxidizing atmosphere.
25S002	E.S.Smirnova, K.V.Frolov, E.V.Sidorova, T.A.Sorokin, O.A.Alekseeva, A.V.Guskov, P.G.Gagarin, and I.A.Gudim, *Acta Crystallogr., Sect. B: Struct. Sci., Cryst. Eng. Mater.* **81**(1),69-83(2025) Structural and magnetic phase transitions in $Eu_{1-x}La_xFe_3(BO_3)_4$ (x=0, 0.18).
25S003	S.Sahih, M.Hemmous, A.Guittoum*, D.Martinez-Blanco, J.A.Blanco, P.Gorria, and M.Sidoumou, *J. Supercond. Novel Magn.* **38**(1),39/1-13(2025) Effect of chromium concentration on the microstructure and magnetic properties of FeCr nanostructured powders prepared by mechanical alloying.
25S004	B.L.D.Santos, A.C.Krohling, K.Krambrock, E.C.Passamani, and W.A.A.Macedo*, *J. Magn. Magn. Mater.* **614**, 172691/1-10(2025) Structural and magnetic properties of Co_2FeGa full-Heusler alloy thin films with low Gilbert damping.
25S005	A.Szegedi, K.Lázár, H.Solt, and M.Popova*, *Surf. Interfaces* **56**,105498/1-11(2025) Peculiar redox properties of SBA-15 supported copper ferrite catalysts promoting total oxidation of a model volatile organic air pollutant.
25S006	IV.Strelnikova, A.S.Ovsyanniko*, A.VPyataev, D.R.Islamov, I.A.Litvinov, P.V.Dorovatovskii, S.E.Solovieva, and I.S.Antipin, *Eur. J. Inorg. Chem.* **28**(3),e202400581/1-6(2025) First evidencing of guest-induced spin transition for dinuclear Fe(III) complex supported by calix[4]arene Schiff base ligand.
25T001	T.Tatarchuk, V.Bilovol, A.Shyichuk, I.Danyliuk, K.Sokolowski, and M.Gajewska, *Appl. Surf. Sci.* **690**, 162610/1-21(2025) Mesoporous Co-Mn ferrites as highly radical-forming catalysts for wet peroxide oxidation of 4-nitrophenol.
25T002	C.Tacconis, S.Dey, C.D.McLaughlin, M.T.Sougrati, C.A.O'Keefe, I.Mikulska, C.P.Grey, and S.E.Dutton*, *Chem. Mater.* **37**(1),463-72(2025) Role of Fe impurity reactions in the electrochemical properties of $MgFeB_2O_5$.
25T003	T.Tatarchuk, A.Shyichuk, V.O.Kotsyubynsky, and N.Danyliuk, *Ceram. Int.* **51**(4),4988-99(2025) Catalytically active cobalt ferrites synthesized using plant extracts: insights into structural, optical, and catalytic properties.
25W001	J.F.Wan, Y.Zhang, N.N.Fu, B.Jiang, H.S.Li, Y.Yin*, and W.M.Zhang, *Sep. Purif. Technol.* **354**(Part_8), 129563/1-8(2025) The influence of Fe-N coordination structure on the formation of reactive species in carbon-based Fenton-like system.

Code	Reference
25W002	Y.Wang, Z.Y.Huang, Z.Yan, Z.C.Lei, H.X.Ma, and C.H.Feng*, *Water Res.* **275**,123193/1-11(2025) Overcoming Fe(III) precipitation barrier in acid mine drainage via a visible light-assisted photo-electrochemical system.
25W003	Z.J.Wu, G.Q.Liu, K.Y.Gao, Z.Y.Lu, and M.Liu*, *J. Alloys Compd.* **1017**,179018/1-10(2025) Magnetic phase transitions and giant magnetocaloric effect in Mn-doped $GdFeO_3$ polycrystalline.
25W004	S.Wittmann, M.M.Murshed*, K.Ghosh, A.Koldemir, R.Pöttgen, C.B.Mendive, and T.M.Gesing, *J. Am. Ceram. Soc.* **108**(2),e20170/1-12(2025) Thermal properties of mullite-type $SnAlBO_4$ and $SnGaBO_4$.
25W005	C.W.Wang, X.B.Peng*, Q.H.Zhang, T.Li, T.Xing, Q.Liu, J.C.Sui, and N.Tsubaki*, *Appl. Catal., B* **361**,124612/1-11(2025) Highly efficient hydrogenation of CO_2 to heavy hydrocarbons via NaFeGa catalysts.
25W006	C.P.Wang, J.T.Yan, T.Y.Li, Y.F.Tang*, Q.Zheng*, and X.F.Li*, *Chem. Eng. J. (Amsterdam, Neth.)* **507**,160355/1-8(2025) Single-atom generation inducing electrochemical transformation during cycling in transition metal sulfides for Na-ion batteries.
25W007	Z.J.Wu, J.B.Yang, C.Y.Wang, Y.F.Xia, and M.Liu*, *J. Magn. Magn. Mater.* **620**,172923/1-7(2025) Structural transformation and magnetic properties of $HoFe_{1-x}Mn_xO_3$ polycrystalline.
25X001	N.Xiao, P.Han*, Z.Q.Chen, and Q.L.Chen*, *J. Colloid Interface Sci.* **680**(Part_A),911-27(2025) Magnetic field and photon co-enhanced S-scheme MXene/In_2S_3/$CoFe_2O_4$ heterojunction for high-performance lithium-oxygen batteries.
25X002	J.J.Xie, N.S.Wu, D.M.Li, S.Y.Xiong, J.J.Dong, R.L.Wang, G.D.Zheng*, and J.G.Li*, *Int. J. Biol. Macromol.* **296**, 139759/1-14(2025) Characterization of Choerospondias axillaris polysaccharide-iron (III) complex and its effect on iron deficiency anemia mice.
25X003	W.H.Xu, S.Q.Wu*, S.Q.Su*, Y.B.Huang, W.W.Zheng, X.P.Zhang, T.C.Ji, K.G.Gao, X.G.Zhou, S.Y.Peng, Q.Chen, M.Tokunaga, Y.H.Matsuda, A.Okazawa*, and O.Sato*, *J. Am. Chem. Soc.* **147**(6),5051-9(2025) Polarization switching from valence trapping in an oxo-bridged trinuclear iron complex.
25Y001	J.Y.Ye, T.J.Gerard, and W.T.Lee*, *Chem. Commun. (Cambridge, U. K.)* **61**(14),2926-40(2025) [2Fe-2S] model compounds.
25Y002	S.Yadav, R.S.Lyons, Z.Readi-Brown, M.A.Siegler, and D.P.Goldberg*, *J. Inorg. Biochem.* **264**,112776/1-9(2025) Influence of the second coordination sphere on O_2 activation by a nonheme iron(II) thiolate complex.
25Y003	Y.Yang, C.H.Wang, S.J.Zheng, J.N.Yao, J.W.Dai, H.J.Chen, C.Han, A.Al-Anazi, H.B.Ji, and Y.Huang*, *Sep. Purif. Technol.* **357**(Part_A),130106/1-12(2025) Activation mechanism of persulfate by Fe_3C-based materials for efficient benzo-a-pyrene abatement in wastewater: the reversed direct electron transfer from persulfate to contaminants.
25Y004	S.Yaroslavtsev, *Nucl. Instrum. Methods Phys. Res., Sect. B* **563**,165669/1-8(2025) Different widths of resonant lines in the Mössbauer spectrum as the result of multidimensional Gaussian distribution.
25Z001	M.Zipkat, A.Koldemir, T.Block, C.Ceniza, T.D.Boyko, S.Kläger, R.M.Pritzl, A.Moewes, R.Pöttgen, S.S.Rudel*, and W.Schnick*, *Chem. - Eur. J.* **31**(10),e202403745/1-11(2025) Scalable bulk synthesis of phase-pure γ-Sn_3N_4 as a model for an argon-flow-mediated metathesis reaction.
25Z002	B.Zawadzki, R.Abid, A.J.Fernandez-Ropero, W.Patkowski, A.Blachowski, K.Matus, M.Krawczyk, D.Lisovytskiy, M.Inger, and A.Srebowata*, *Fuel* **380**,133170/1-11(2025) Effect of iron oxidation state on the catalytic performance of Fe/C in liquid phase flow hydrogenation of 2-butyne-1,4-diol.
25Z003	Z.Zhang, X.Wang, Y.Q.Li, L.Tang*, and Zhang*, *Appl. Surf. Sci.* **691**,162581/1-11(2025) Unveiling light-assisted non-radical dominated sulfadiazine removal in iron-based bimetallic oxide activation of peroxymonosulfate.

Source	Absorber	Temp	IS	QS	Comments	Code
Eu-151 21.60 keV Transition						
EuF_3(IS/EuF_3)	$EuZnBi_2$	v	--	--	observed a spin reorientation near 15 K, below T_N=20 K and at cooling through 11 K the onset of an incommensurate sinusoidally modulated structure that progressively squares up on further cooling	25R001
Fe-57 14.40 keV Transition: Biological Compounds						
Rh(IS/α-Fe)	bacterial cytochrome c peroxidase from Nitrosomonas europaea (Ne bCcP) before and after reaction with H_2O_2	4	--	--	identified 3 species of 6-coordinate Fe^{II} (S=0) or Fe^{III} (S=1/2) in E and P hemes with the ratio of total E (Fe^{II}+Fe^{III}) to P of 62/38 before H_2O_2-reaction, and S=1/2 Fe^{III} species in E and P hemes, compound 2 and compound 1 in amounts relative to total iron of 56%, 16%, 7%, 11% after reaction	25H006
xx(IS/α-Fe)	choerospondias axillaris polysaccharide-iron (III) complex	298	0.34	0.80	determined the IS and QS of octa-Fe(III) similar to other polysaccharide-iron (III) complexes known to possess a β-FeOOH structure	25X002
Rh(IS/α- Fe)	clusters of $NiFe_4S_4$ and $Ni_2Fe_3S_4$ (in [Na(15-crown-5)·Et_2O][IMesNi $Fe_4S_4(N(SiMe_3)_2)_4$], and in $Na(THF)_2(IPrNi)_2((Me_3Si)_2NFe)_2$ FeS_4)	80	--	--	revealed that Fe oxidation states in $NiFe_4S_4$ are $Fe^{2.5+}$(4 species) and that $Ni_2Fe_3S_4$ have one Fe^{3+} and two Fe^{2+}	24F019
Rh(IS/α-Fe)	$CoFe_2O_4$ synthesized using Ginkgo Biloba leaves, flax seeds, tomato juice, and persimmon fruit	300	--	--	determined the cation distribution and ratio of magnetically-split and spm-doublet fractions	25T003
Rh(IS/α-Fe)	Fe-containing proteins, supramolecular structures, microbial cells/tissues and biomedical reagents	v	--	--	reviewed Mössbauer spectroscopy basics and contributions to biomedical sciences	25H007
Rh(IS/α-Fe)	Fe@Fe_3O_4	300	--	--	identified α-Fe sextet, Fe_3O_4 sextets, and spm-oxide doublet	25C005
Rh(IS/α- Fe)	garnets $Y_{3-x}Cd_xFe_5O_{12}$ (x=0, 0.02, 0.04, 0.08, 0.12, 0.2)	v	--	--	Cd^{2+} prefers to occupy the tetrahedral site which can give place to the migration of some Fe^{3+} to the octahedral site	21A044
Rh(IS/α-Fe)	model compounds enclosing the [2Fe–2S] cores	v	--	--	reviewed the isomer shift and quadrupole splitting exhibiting different iron oxidation states such as $[2Fe–2S]^{2+}$ ([Fe^{III}-Fe^{III}]) and the mixed-valent form $[2Fe–2S]^{1+}$ ([Fe^{III}-Fe^{II}]) and $[2Fe–2S]^{0}$ ([Fe^{II}-Fe^{II}])	25Y001
Rh(IS/α-Fe)	periplasmic heme-c enzyme cis-trans isomerase purified from Pseudomonas aeruginosa (Pa-cti)	77	0.46	1.22	confirmed the presence of an octahedral low-spin ferrous iron (Fe^{II}, S=0)	25M002
Rh(IS/α- Fe)	superparamagnetic iron oxide nanoparticles	300	--	--	relaxation-broadened spectrum analysis with Tjon and Blume model revealed the fluctuation frequency f of 123 MHz	25K013
Rh(IS/α-Fe)	β-hematin synthesized in aqueous-acetate medium and aqueous-only medium	v	--	--	identified the rates of spin-spin relaxation using Blume model and explained the increased spectral asymmetry for the aqueous-only medium synthesis	25H005
xx(IS/α-Fe)	γ-Fe_2O_3 biosynthesized with decoction and powder from natural leaves	15	--	--	identified two magnetic components attributed to A site (tetrahedral) and B site (octahedral)	25A006
Fe-57 14.40 keV Transition: Catalysts						
Rh(IS/α-Fe)	(EmL)Fe(N_3) (Em: 1,1,7,7-tetraethyl-1,2,3,5,6,7-hexahydro-3,3,5,5-tetramethyl-s-indacene)	90	0.72	0.55	identified three-coordinate three-coordinate, high-spin, terminal, azido, Fe(II)	25O001
Rh(IS/α-Fe)	(EmL)FeCl (Em: 1,1,7,7-tetraethyl-1,2,3,5,6,7-hexahydro-3,3,5,5-tetramethyl-s-indacene)	90	0.74	0.30	identified three-coordinate HS Fe^{II} (coordinated by Cl and 2N)	25O001
Rh(IS/α-Fe)	catalyst of Fe/C with commercial amorphous carbon produced by Norit company	300	--	--	identified the major doublet assigned to amorphous carbon, and alpha-Fe, and spm-Fe_2O_3	25Z002
Rh(IS/α- Fe)	catalysts AuPd^{57}Fe/TiO_2	v	--	--	identified doublets assigned to Fe^0, Fe^{2+} and two kinds of Fe^{3+} species (oligomers and isolated)	25L009
Rh(IS/α- Fe)	clusters of $NiFe_4S_4$ and $Ni_2Fe_3S_4$ (in [Na(15-crown-5)·Et_2O][IMesNi $Fe_4S_4(N(SiMe_3)_2)_4$], and in $Na(THF)_2(IPrNi)_2((Me_3Si)_2NFe)_2$ FeS_4)	80	--	--	revealed that Fe oxidation states in $NiFe_4S_4$ are $Fe^{2.5+}$(4 species) and that $Ni_2Fe_3S_4$ have one Fe^{3+} and two Fe^{2+}	24F019

Source	Absorber	Temp	IS	QS	Comments	Code
Rh(IS/α- Fe)	core-shell layered Mesoporous Spherical iron-based carbon catalyst (Fe/C–MS) and Nano-Plate structured iron-based carbon (Fe/C–NP)	v	--	--	identified 2 sextets for Fe/C–NP, assigned to maghemite and magnetite, whereas 2 sextets + spm doublet for Fe/C–MS	25L007
xx	$Co_xNi_{(0.4-x)}Fe_{2.6}O_4$ spinels for x=0, 0.1, 0.2, 0.3 and 0.4	300	--	--	isomer shifts and hyperfine fields evidence high-spin Fe(III)	20V020
Rh(IS/α-Fe)	Fe-N-C catalysts calcined at 600◦C, 700◦C, and 800 ◦C	300	--	--	identified the doublets D1 and D2 with the narrow to broader doublet area ration increasing as the calcination temperature increases	25W001
Rh(IS/α- Fe)	Fe/ZIF-8 calcined at 900 ◦C for 3 h in an argon atmosphere without and with Vitamin C	300	--	--	identified species Fe^{II}-N_4, O_x-Fe^{III}-N_4, and phases of iron oxides, α-Fe and Fe_3C	21H029
Rh(IS/α-Fe)	Fe_3C-related catalysts	300	--	--	undefined Mössbauer spectra velocity scale	25Y003
Rh(IS/α-Fe)	ferrites $Co_xMn_{1-x}Fe_2O_4$ (x=0, 0.1, 0.3, 0.5, 0.7, 1) as catalysts for wet peroxide oxidation of 4-nitrophenol	v	--	--	estimated the distribution of cations in octahedral and tetrahedral positions and a superparamagnetic fraction	25T001
Rh(IS/α-Fe)	iron-based bimetallic oxide with peroxymonosulfate	300	--	--	identified a sextet of oxide and after photoexcitation a new singlet line appears at 0.13 mm/s assigned to Fe^{4+}	25Z003
Rh(IS/α-Fe)	NaFe and NaFeGa catalyst	300	--	--	identified Fe_3O_4 and alpha-Fe phases and minor Fe2+and Fe^{3+} doublets hydrogenation of CO_2 to heavy hydrocarbons and Fe_3O_4 and x-Fe_5C_2 and Fe^{3+} doublet after	25W005
Rh(IS/α-Fe)	periplasmic heme-c enzyme cis-trans isomerase purified from Pseudomonas aeruginosa (Pa-cti)	77	0.46	1.22	confirmed the presence of an octahedral low-spin ferrous iron (Fe^{II}, S=0)	25M002
Rh(IS/α-Fe)	reduced and spent Fe foam catalysts promoted with Na or K or Rb or Cs nitrate impregnation	300	--	--	identified magnetic phases of χ-Fe_5C_2, Fe_3C, α-Fe, and doublets Fe^{2+}(spm), Fe^{3+}(spm)	25A007
Rh(IS/α-Fe)	silica (SBA-15) -supported copper ferrite catalysts after impregnating salt decomposition in air and in NO/He mixture and pretreatments in 380 ◦C in vacuum, H_2 or air	300	--	--	identified three doublets of Fe^{3+} and, additionally after 380 ◦C in H_2, also three doublets of Fe^{2+}	25S005
<u>Fe-57 14.40 keV Transition: FERROMAGNETIC</u>						
Rh(IS/α-Fe)	$Co_xFe_{(1-x)}Al$ Heusler alloy	300	--	--	identified a predominant sextet indicative of ferromagnetic order	25A005
Rh(IS/α-Fe)	$Fe_2Cr_{1-x}Co_xSi$ (x=0, 0.5) Heusler alloy	300	--	--	observed one sextet and one doublet for x=0, however, 3 sextets and a singlet for x=0.5	25J004
Rh(IS/α-Fe)	$Fe^{II}(BPA^{Me2}S)Br$ frozen in THF	80	0.93	3.29	identified HS Fe(II) in coordination 5 (Br, S and 3N)	25Y002
Rh(IS/α-Fe)	$KSr_2(FeNb_4)O_{15-\delta}$	v	--	--	identified a sextet (64%) and a doublet (36%) representing the magnetic and paramagnetic sublattices	25N003
Rh(IS/α-Fe)	thin films of Co_2FeGa Heusler alloy deposited at 300 ◦C and 600 ◦C and annealed at the same temperature for 0 and 60 min	300	--	--	the peak value of P(B_{hf}) distributions about 31 T strongly suggests an ordered L21-type structure for the major part of the samples	25S004
Rh(IS/α-Fe)	γ-Fe_2O_3	300	--	--	identified 2 equipopulated sharp sextet sub-spectra, with B_{hf} of 47.5 and 49.5 T, and a third broadened sextet distribution sub-spectrum attributed to relaxation effects and/or P(B_{hf}) asymmetric distribution caused by structural disorder	25P004
<u>Fe-57 14.40 keV Transition: Frozen Solutions</u>						
Rh(IS/α-Fe)	bacterial cytochrome c peroxidase from Nitrosomonas europaea (Ne bCcP) before and after reaction with H_2O_2	4	--	--	identified 3 species of 6-coordinate Fe^{II} (S=0) or Fe^{III} (S=1/2) in E and P hemes with the ratio of total E (Fe^{II}+Fe^{III}) to P of 62/38 before H_2O_2-reaction, and S=1/2 Fe^{III} species in E and P hemes, compound 2 and compound 1 in amounts relative to total iron of 56%, 16%, 7%, 11% after reaction	25H006
Rh(IS/α- Fe)	clusters of $NiFe_4S_4$ and $Ni_2Fe_3S_4$ (in [Na(15-crown-5)·Et_2O][IMesNi $Fe_4S_4(N(SiMe_3)_2)_4$], and in $Na(THF)_2(IPrNi)_2((Me_3Si)_2NFe)_2$ FeS_4)	80	--	--	revealed that Fe oxidation states in $NiFe_4S_4$ are $Fe^{2.5+}$(4 species) and that $Ni_2Fe_3S_4$ have one Fe^{3+} and two Fe^{2+}	24F019

Source	Absorber	Temp	IS	QS	Comments	Code
Rh(IS/α-Fe)	Fe-containing proteins, supramolecular structures, microbial cells/tissues and biomedical reagents	v	--	--	reviewed Mössbauer spectroscopy basics and contributions to biomedical sciences	25H007
Rh(IS/α-Fe)	$Fe^{II}(BPA^{Me2}S)Br$ frozen in THF	80	0.93	3.29	identified HS Fe(II) in coordination 5 (Br, S and 3N)	25Y002
Rh(IS/α-Fe)	solid $[Fe_2(CO)_{10}]^{2+}([AsF_6]^-)_2$	14	0.03	0.23	identified a Fe(I) dication with a very strong dependence of the quadrupole splitting at short distances	25B008
Fe-57 14.40 keV Transition: Glasses and Amorphous Substances						
Rh(IS/α-Fe)	black volcanic ashes of the tephri–phonolite'Pozzolane Nere' magma from the Colli Albani (Rome, Italy)	300	--	--	identified three paramagnetic components attributed to Fe^{2+} and Fe^{3+} glass sites and determined the relative Fe^{2+} and Fe^{3+} fractions	25F002
Rh(IS/α- Fe)	phosphosilicate wastes produced by adding a borosilicate frit	300	--	--	found evidence of hematite formation for very small (2.5 and 3%) frit addition, but observed that the hematite formation was suppressed with the additions of 5 wt % –15 wt % borosilicate frit	25E003
Rh(IS/α-Fe)	radioactive waste without and with BN in various proportions	300	--	--	identified the doublets of Fe^{2+} and Fe^{3+} and determined the ratio Fe^{3+}/Fe(total) decreasing from 1.00 to 0.76 to 0.67 and to 0.45, as the mass proportion of BN added to make the glass increased from 0 to $BN_{0.25}$, $BN_{0.5}$, and $BN_{0.75}$ in feeds	25R003
Fe-57 14.40 keV Transition: Inorganic Cyanides						
Rh(IS/α- Fe)	metal-organic framework after adsorption of the pyrrole molecules, $\{Fe(pz)[Ni\text{-}(CN)_4]\}\supset Py^t$ ($1\supset Py^t$)	v	--	--	identified a doublet of HS Fe(II) at 300 K and two doublets at 80 K, assigned to LS Fe(II and HS Fe(II) and observed that the spin transition occurs, ranging from ca.300 to 250 K	25L008
Fe-57 14.40 keV Transition: Inorganic Oxides						
Rh(IS/α-Fe)	120 nm thick epitaxial $BaFe_{12}O_{19}$ film on a (0001) SGMZ substrate, and 60 nm thick α-iron film epitaxially grown on (100) MgO	300	--	--	confirmed that magnetization in epitaxial iron on (100) MgO is along the ⟨00⟩ direction, and in $BaFe_{12}O_{19}$ it is perpendicular to the plane (0001) of the substrate of $Sr_{1.03}Ga_{10.81}Mg_{0.58}Zr_{0.58}O_{19}$	25L006
Rh(IS/α- Fe)	$Ba_{0.5}Sr_{0.5}Pd_{3x}Fe_{12-2x}O_{19}$ ($x \leq 0.1$)	300	--	--	determined B_{hf}, which for different crystallographic sites was ranked as $4f_2$>2a>$4f_1$>12k>2b	25A004
Rh(IS/α-Fe)	$Bi_2Fe_4O_9$ nanostructures	77	--	--	identified magnetically split an collapsed components assigned mainly to $Bi_2Fe_4O_9$, and minority to $BiFeO_3$	25M001
Rh(IS/α-Fe)	black volcanic ashes of the tephri–phonolite'Pozzolane Nere' magma from the Colli Albani (Rome, Italy)	300	--	--	identified three paramagnetic components attributed to Fe^{2+} and Fe^{3+} glass sites and determined the relative Fe^{2+} and Fe^{3+} fractions	25F002
Rh(IS/α-Fe)	catalyst of Fe/C with commercial amorphous carbon produced by Norit company	300	--	--	identified the major doublet assigned to amorphous carbon, and alpha-Fe, and spm-Fe_2O_3	25Z002
Rh(IS/α- Fe)	catalysts $AuPd^{57}Fe/TiO_2$	v	--	--	identified doublets assigned to Fe^0, Fe^{2+} and two kinds of Fe^{3+} species (oligomers and isolated)	25L009
xx(IS/α-Fe)	choerospondias axillaris polysaccharide-iron (III) complex	298	0.34	0.80	determined the IS and QS of octa-Fe(III) similar to other polysaccharide-iron (III) complexes known to possess a β-FeOOH structure	25X002
xx	coal mine drainage sludge	300	--	--	identified two doublets, both assigned to Fe(III)	25C008
Rh(IS/α-Fe)	$CoFe_2O_4$ nanoparticles	90	0.511	0	as sintering temperature increases from 500 to 1000 degree C the parameter γ (degree of cation inversion) increases from 0.55 to 0.83	25B006
Rh(IS/α-Fe)	$CoFe_2O_4$ synthesized using Ginkgo Biloba leaves, flax seeds, tomato juice, and persimmon fruit	300	--	--	determined the cation distribution and ratio of magnetically-split and spm-doublet fractions	25T003
Rh(IS/α-Fe)	composite formed from 70% $LaSr(CoFe)_{1/2}O_4$ and 30% $(LaSr)_{1/2}(CoFe)_{1/2}O_3$	v	--	--	identified three groups of iron species: Fe^{4+}, $Fe^{(3+\delta_1)+}$ and $Fe^{(3-\delta_2)+}$	25F004
Rh(IS/α-Fe)	composite of $Ti_3C_2/In_2S_3/CoFe_2O_4$	300	--	--	identified two sextets assigned to Fe^{3+} in tetrahedral and octahedral sites and a doublet of HS Fe^{2+} in tetrahedral sites	25X001
Rh(IS/α- Fe)	composition $MgSiO_3$ +$FeAlO_3$ (60: 40) before and after grain growth at 2000 K and 27 GPa	300	0.421	1.015	observed the increase of IS up to 0.434 mm/s and decrease in QS to 0.988 mm/s and no detectable ferrous iron	24F018
Rh(IS/α- Fe)	core-shell layered Mesoporous Spherical iron-based carbon catalyst (Fe/C–MS) and Nano-Plate structured iron-based carbon (Fe/C–NP)	v	--	--	identified 2 sextets for Fe/C–NP, assigned to maghemite and magnetite, whereas 2 sextets + spm doublet for Fe/C–MS	25L007

Source	Absorber	Temp	IS	QS	Comments	Code
xx	$Co_xNi_{(0.4-x)}Fe_{2.6}O_4$ spinels for x=0, 0.1, 0.2, 0.3 and 0.4	300	--	--	isomer shifts and hyperfine fields evidence high-spin Fe(III)	20V020
Cr(IS/α-Fe)	$EuFe_3(BO_3)_4$ and $Eu_{0.82}La_{0.18}Fe_3(BO_3)_4$	v	--	--	obtained the Neel temperatures (T_N) of 34.57 and 32.22 K with high accuracy, however no separate contributions resolved from the two structural positions of iron ions Fe1 and Fe2	25S002
Rh(IS/α- Fe)	Fe/ZIF-8 calcined at 900 ◦C for 3 h in an argon atmosphere without and with Vitamin C	300	--	--	identified species Fe^{II}-N_4, O_x-Fe^{III}-N_4, and phases of iron oxides, α-Fe and Fe_3C	21H029
Rh(IS/α-Fe)	Fe_3O_4 microparticles hydrothermally synthesized with different $(PO_4)/(SO_4)$ anions ratio	300	--	--	identified 5 sextets assigned to metal Fe and a mixture of stoichiometric and non-stoichiometric Fe_3O_4	25N002
Rh(IS/α-Fe)	$Fe@Fe_3O_4$	300	--	--	identified α-Fe sextet, Fe_3O_4 sextets, and spm-oxide doublet	25C005
Rh(IS/α- Fe)	ferrite $Cd_{0.5}Cu_{0.5}Cr_xFe_{2-x}O_4$ for x=0.1, 0.2, 0.3, 0.4, and 0.5	v	--	--	determined the Fe occupancies in tetrahedral site and octahedral site and also Cd and Cu and Cr cation distribution	25E002
Rh(IS/α-Fe)	ferrites $Co_xMn_{1-x}Fe_2O_4$ (x=0, 0.1, 0.3, 0.5, 0.7, 1) as catalysts for wet peroxide oxidation of 4-nitrophenol	v	--	--	estimated the distribution of cations in octahedral and tetrahedral positions and a superparamagnetic fraction	25T001
Rh(IS/α-Fe)	ferroborates $SmFe_{3-x}Al_x(BO_3)_4$ with x=0, 0.07, and 0.28	v	--	--	identified broadened S1, S2, S3 sextet components approximated within the multilevel spin relaxation mode below T_N decreasing from 32 to 28 K with increasing x within the studied range of x	25F003
Rh(IS/α- Fe)	garnets $Y_{3-x}Cd_xFe_5O_{12}$ (x=0, 0.02, 0.04, 0.08, 0.12, 0.2)	v	--	--	Cd^{2+} prefers to occupy the tetrahedral site which can give place to the migration of some Fe^{3+} to the octahedral site	21A044
Rh(IS/α-Fe)	$GdFe_{1-x}Mn_xO_3$ (x=0.00, 0.25, 0.50)	v	--	--	as x increases the sextets appear with Fe nearest-neighbor Mn ions, with the internal field following the relation $H_n=H_0(1-n\Delta H)$ with ΔH=1.94 T and H_0=50.87T	25W003
Rh(IS/α-Fe)	German bentonite clay and Italian red modified montmorillonite clay	300	--	--	identified mainly hematite in German clay and minor illite/kaolinite phase, and main kaolinite/illite in Italian clay	25N001
Rh(IS/α-Fe)	high-entropy spinel-type oxide $(Zn_{0.25}Mg_{0.25}Co_{0.25}Cu_{0.25})Fe_2O_4$ and lithiated oxyhalides $Li_{0.5}(Zn_{0.25}Mg_{0.25}Co_{0.25}Cu_{0.25})_{0.5}Fe_2O_{3.5}F_{0.5}$, $Li_{0.5}(Zn_{0.25}Mg_{0.25}Co_{0.25}Cu_{0.25})_{0.5}Fe_2O_{3.5}Cl_{0.5}$	300	--	--	observed two sextets identified with tetrahedral and octahedral sites of the spinel	25P001
Rh(IS/α-Fe)	$HoFe_{1-x}Mn_xO_3$(x=0, 0.2, 0.4, 0.5, 0.6, 0.8 and 1)	300	--	--	confirmed that Mn doping weakens the Fe^{3+}-Fe^{3+} magnetic interactions, leading to a gradual transformation of the magnetic sextet into a paramagnetic doublet, indicating a reduction in the magnetic ordering temperature to below room temperature as Mn doping concentration increases, with T_N reaching near room temperature at x=0.5	25W007
Rh(IS/α-Fe)	iron ore from the Wugang and Hengyang BIFs in China	300	--	--	identified hematite and maghemite phases in different proportions	25K012
Rh(IS/α- Fe)	iron oxide nanoparticles with a mean size of 11 nm and narrow size distribution (σ=0.28)	300	--	--	relaxational spectra fit with multiple sextets and a collapsed hump	25K014
Rh(IS/α-Fe)	iron-based bimetallic oxide with peroxymonosulfate	300	--	--	identified a sextet of oxide and after photoexcitation a new singlet line appears at 0.13 mm/s assigned to Fe^{4+}	25Z003
Rh(IS/α-Fe)	$KSr_2(FeNb_4)O_{15-\delta}$	v	--	--	identified a sextet (64%) and a doublet (36%) representing the magnetic and paramagnetic sublattices	25N003
Rh(IS/α- Fe)	$LiFePO_4$ (black powder for recycling) and $FePO_4/Li_3Fe_2(PO_4)_3$ (leaching residue) and $FePO_4$ (recovered)	300	--	--	isomer shifts and QS for Fe^{3+} in leaching resudue are larger than IS.QS parameters expected for Fe^{3+} in $FePO_4$	25C007
Rh(IS/α-Fe)	$MgFeB_2O_5$ cathode discharged and during charge at 3V and 4.2V	300	--	--	identified mainly two HS Fe^{2+} doublets and a minor Fe metal impurity sextet and demonstrated the appearance of third doublet at highly charged state	25T002
Rh(IS/α-Fe)	nanoparticles of $Ni_{0.5}Zn_{0.5}Fe_2O_4$ composites with MWCNTs	300	--	--	undefined one or two sextets, a collapsed component, spm-doublet and a single line assigned to γ-Fe	25B007
Rh(IS/α-Fe)	narrowly sieved iron particles with a mean diameter of 49 μm in the progress if oxidation in laminar flow reactor	300	--	--	determined the bulk composition of the quenched particles with respect to α-Fe and its three oxides FeO, Fe_3O_4, and Fe_2O_3 as the function of extraction position at 25, 28, 33, 38, 43, 48, 88, 137 and 186mm of the height above burner	25S001

Source	Absorber	Temp	IS	QS	Comments	Code
Rh(IS/α-Fe)	NbC-Fe and NbC-FeNi milled powders, and in NbC-Fe and NbC-Fe-Mo_2C cermets, and NbC-FeNi and NbC-FeNi-Mo_2C cermets	v	--	--	observed magnetic sextets in both NbC-Fe and NbC-FeNi milled powders and in NbC-Fe and NbC-Fe-Mo_2C cermets with B_{hf} of 29.4 T to 33.1 T, however, B_{hf}=0 for NbC-FeNi and NbC-FeNi-Mo_2C cermets with gamma-FeNi phase	25P003
Rh(IS/α- Fe)	phosphosilicate wastes produced by adding a borosilicate frit	300	--	--	found evidence of hematite formation for very small (2.5 and 3%) frit addition, but observed that the hematite formation was suppressed with the additions of 5 wt % –15 wt % borosilicate frit	25E003
Rh(IS/α-Fe)	photo-electrochemically (PEC)-synthesized and H_2O_2-produced acid mine drainage precipitates	300	--	--	identified doublets characteristic of schwertmannite	25W002
Rh(IS/α-Fe)	products from the reactions of dimethylarsenate incorporated into ferrihydrite with 1 mM Fe(II) at pH 4 and 7	6.2	--	--	revealed after reaction that 52.0–53% of the ferrihydrite in the coprecipitate is transformed to lepidocrocite	25C006
Rh(IS/α-Fe)	radioactive waste without and with BN in various proportions	300	--	--	identified the doublets of Fe^{2+} and Fe^{3+} and determined the ratio Fe^{3+}/Fe(total) decreasing from 1.00 to 0.76 to 0.67 and to 0.45, as the mass proportion of BN added to make the glass increased from 0 to $BN_{0.25}$, $BN_{0.5}$, and $BN_{0.75}$ in feeds	25R003
Rh(IS/α- Fe)	$ScMn_{0.996}Fe_{0.004}O_3$	300	--	--	identified 2D character of magnetic ordering below T_N=131 K from reduced $B_{hf} \approx 467$ kOe at 15K and from the exponent in the temperature dependence of B_{hf}	24S082
Rh(IS/α-Fe)	silica (SBA-15) -supported copper ferrite catalysts after impregnating salt decomposition in air and in NO/He mixture and pretreatments in 380 ◦C in vacuum, H_2 or air	300	--	--	identified three doublets of Fe^{3+} and, additionally after 380 ◦C in H_2, also three doublets of Fe^{2+}	25S005
Rh(IS/α-Fe)	solid solutions $(1-x)(Na_{0.5}K_{0.5})NbO_{3-x}BiFeO_3$ with $0.85 \le x \le 0.95$	v	--	--	identified the Fe^{3+} species with a certain number of Nb^{5+} ions in the local Fe^{3+} environment, which leads to a decrease in B_{hf} values, thus producing six partial spectral contribution S2-S7, and a doublet D1 assigned to the impurity phase of $Bi_{25}FeO_{39}$	25M003
Rh(IS/α- Fe)	superparamagnetic iron oxide nanoparticles	300	--	--	relaxation-broadened spectrum analysis with Tjon and Blume model revealed the fluctuation frequency f of 123 MHz	25K013
Rh(IS/α- Fe)	xFe_2O_3–(100–x)P_2O_5 glasses containing 25 to 40 mol% Fe_2O_3 synthesized by melt quenching and a crystalline sample for x=50	300	--	--	identified 3 sites of Fe^{2+} and 1 site of Fe^{3+} in glass samples, while 5 sites of Fe^{2+} and 2 sites of Fe^{3+} in crystalline sample	25D004
Rh(IS/α- Fe)	Y_2FeTaO_7, Sm_2FeTaO_7, $Y_2Fe_{0.7}Mg_{0.3}TaO_7$,$Y_{1.85}Mg_{0.15}FeTaO_7$ and $Y_{1.8}Fe_{1.2}TaO_7$	300	--	--	identified a subspectrum assigned to eight-coordinated site and 2 subspectra assigned to six-coordinated sites, and determined the Fe distributions between these 3 sites	24E009
Rh(IS/α-Fe)	zinc ferrite covering layers on 3D-printed cylinders of CL20ES steel	300	--	--	identified the paramagnetic components of γ-Fe and Fe^{3+} ; the latter shows QS and FWHM decreasing with increasing annealing temperature from room temperature to 900 ◦C	24O011
Rh(IS/α-Fe)	γ-Fe_2O_3	300	--	--	identified 2 equipopulated sharp sextet sub-spectra, with B_{hf} of 47.5 and 49.5 T, and a third broadened sextet distribution sub-spectrum attributed to relaxation effects and/or P(B_{hf}) asymmetric distribution caused by structural disorder	25P004
xx(IS/α-Fe)	γ-Fe_2O_3 biosynthesized with decoction and powder from natural leaves	15	--	--	identified two magnetic components attributed to A site (tetrahedral) and B site (octahedral)	25A006
<u>Fe-57 14.40 keV Transition: Inorganic Sulfides</u>						
Rh(IS/α-Fe)	composite of $Ti_3C_2/In_2S_3/CoFe_2O_4$	300	--	--	identified two sextets assigned to Fe^{3+} in tetrahedral and octahedral sites and a doublet of HS Fe^{2+} in tetrahedral sites	25X001
Rh(IS/α-Fe)	Fe_3O_4 microparticles hydrothermally synthesized with different $(PO_4)/(SO_4)$ anions ratio	300	--	--	identified 5 sextets assigned to metal Fe and a mixture of stoichiometric and non-stoichiometric Fe_3O_4	25N002
Rh(IS/α-Fe)	FeS_2@NC composite electrode at 3V in initial cycle and in 2nd cycle	v	--	--	identified FeS_2, FeS_x and alpha-Fe	25W006
<u>Fe-57 14.40 keV Transition: Inorganic Sulphates</u>						
Rh(IS/α-Fe)	Fe_3O_4 microparticles hydrothermally synthesized with different $(PO_4)/(SO_4)$ anions ratio	300	--	--	identified 5 sextets assigned to metal Fe and a mixture of stoichiometric and non-stoichiometric Fe_3O_4	25N002

Source	Absorber	Temp	IS	QS	Comments	Code
Rh(IS/α-Fe)	iron-based bimetallic oxide with peroxymonosulfate	300	--	--	identified a sextet of oxide and after photoexcitation a new singlet line appears at 0.13 mm/s assigned to Fe^{4+}	25Z003
Rh(IS/α- Fe)	$LiFePO_4$ (black powder for recycling) and $FePO_4/Li_3Fe_2(PO_4)_3$ (leaching residue) and $FePO_4$ (recovered)	300	--	--	isomer shifts and QS for Fe^{3+} in leaching resudue are larger than IS.QS parameters expected for Fe^{3+} in $FePO_4$	25C007
Rh(IS/α-Fe)	photo-electrochemically (PEC)-synthesized and H_2O_2-produced acid mine drainage precipitates	300	--	--	identified doublets characteristic of schwertmannite	25W002
Rh(IS/α-Fe)	water-soluble μ-S nitrosyl iron complex with acetylcysteine $[Fe_2(C_5H_8NO_3S)_2(NO)_4]\bullet 2H_2O$	295	0.0872	1.0407	identified a unusually sharp doublet from the low-spin state of d^6/d^7 dimer delocalized on Mössbauer timescale, but showing an S=1/2 EPR signal	25R002
Fe-57 14.40 keV Transition: Irradiation Experiments						
Rh(IS/α-Fe)	radioactive waste without and with BN in various proportions	300	--	--	identified the doublets of Fe^{2+} and Fe^{3+} and determined the ratio Fe^{3+}/Fe(total) decreasing from 1.00 to 0.76 to 0.67 and to 0.45, as the mass proportion of BN added to make the glass increased from 0 to $BN_{0.25}$, $BN_{0.5}$, and $BN_{0.75}$ in feeds	25R003
Fe-57 14.40 keV Transition: Metals and Alloys						
Rh(IS/α-Fe)	$(Fe_{63}Ni_{37})_{89}B_{11}$ (FeNiB) powder alloys before and after milling for 36 hours	300	--	--	identified a singlet (assigned to non-magnetic Fe-rich gamma-FCC) and four sextets assigned to magnetic Ni-rich gamma-FCC(sextet 1) and alpha-BCC (Sextet-2) and oP-(Fe,Ni)B (Sextet-3 and Sextet-4) structural phases	25G008
Rh(IS/α-Fe)	as-quenched $Fe_{83.5}Si_3B_{10-x}P_{2+x}Cu_{1.5}$ (x=0, 3, 6 & 8 at.%) amorphous alloys	300	--	--	observed the increase in A23, representing the intensity ratio between the second and third lines, as the B/P ratio decreases	25H009
Rh(IS/α- Fe)	catalysts $AuPd^{57}Fe/TiO_2$	v	--	--	identified doublets assigned to Fe^0, Fe^{2+} and two kinds of Fe^{3+} species (oligomers and isolated)	25L009
Rh(IS/α-Fe)	$Co_xFe_{(1-x)}Al$ Heusler alloy	300	--	--	identified a predominant sextet indicative of ferromagnetic order	25A005
Rh(IS/α-Fe)	$Fe_2Cr_{1-x}Co_xSi$ (x=0, 0.5) Heusler alloy	300	--	--	observed one sextet and one doublet for x=0, however, 3 sextets and a singlet for x=0.5	25J004
xx(IS/α-Fe)	$Fe_{80.5}B_{9.5+x}P_8Cu_{1.5-x}Nb_{0.5}$ (x = 0, 0.4, & 0.8 at%) alloy ribbons in both quenched and relaxed states	300	--	--	observed rightward shift of the low-field P(B_{hf}) peak attributed to the migration of Cu out of the coordination shell surrounding Fe atoms, facilitating the formation of Cu clusters and thereby increasing the B_{hf} values of Fe	25H008
Rh(IS/α-Fe)	$Fe@Fe_3O_4$	300	--	--	identified α-Fe sextet, Fe_3O_4 sextets, and spm-oxide doublet	25C005
xx	iron-silicon alloys containing 5, 6, and 8 at % Si, subjected to thermal magnetic treatment in a dc magnetic field	v	--	--	determined the extent of induced magnetic anisotropy (the relative volume fractions of iron atomic magnetic moments aligned along the 100 axes in the plane)	24E008
Rh(IS/α-Fe)	mechanically alloyed $Fe_{100-x}Cr_x$ with x=2.5, 7.5, 12.5, 17.5 and 20 at.%	300	--	--	determined the B_{hf} distribution changes with Cr content	25S003
Rh(IS/α-Fe)	$MgFeB_2O_5$ cathode discharged and during charge at 3V and 4.2V	300	--	--	identified mainly two HS Fe^{2+} doublets and a minor Fe metal impurity sextet and demonstrated the appearance of third doublet at highly charged state	25T002
Rh(IS/α-Fe)	narrowly sieved iron particles with a mean diameter of 49 μm in the progress if oxidation in laminar flow reactor	300	--	--	determined the bulk composition of the quenched particles with respect to α-Fe and its three oxides FeO, Fe_3O_4, and Fe_2O_3 as the function of extraction position at 25, 28, 33, 38, 43, 48, 88, 137 and 186mm of the height above burner	25S001
Rh(IS/α-Fe)	NbC-Fe and NbC-FeNi milled powders, and in NbC-Fe and NbC-Fe-Mo_2C cermets, and NbC-FeNi and NbC-FeNi-Mo_2C cermets	v	--	--	observed magnetic sextets in both NbC-Fe and NbC-FeNi milled powders and in NbC-Fe and NbC-Fe-Mo_2C cermets with B_{hf} of 29.4 T to 33.1 T, however, B_{hf}=0 for NbC-FeNi and NbC-FeNi-Mo_2C cermets with gamma-FeNi phase	25P003
Rh(IS/α-Fe)	thin films of Co_2FeGa Heusler alloy deposited at 300 ◦C and 600 ◦C and annealed at the same temperature for 0 and 60 min	300	--	--	the peak value of P(B_{hf}) distributions about 31 T strongly suggests an ordered L21-type structure for the major part of the samples	25S004
xx(IS/α- Fe)	$Y(Fe_{0.83}Co_{0.17})z$ (z=10.5, 11.0, 11.25,11.5, 12.0, 12.5, 13.0, 13.5, 14.0, 15.0, 16.0, and 17.0)	300	--	--	identified B_{hf} for the phases d-$Y_2(Fe, Co)_{17}$ and α-(Fe, Co) and correlated B_{hf} with magnetic moments; revealed from hyperfine fields that the structures similar to $ThMn_{12}$ structure tend to have larger magnetic moments than $TbCu_7$ structure	20S095
Rh(IS/α-Fe)	zinc ferrite covering layers on 3D-printed cylinders of CL20ES steel	300	--	--	identified the paramagnetic components of γ-Fe and Fe^{3+} ; the latter shows QS and FWHM decreasing with increasing annealing temperature from room temperature to 900 ◦C	24O011

Source	Absorber	Temp	IS	QS	Comments	Code
Fe-57 14.40 keV Transition: Miscellaneous Inorganic Compounds						
Rh(IS/α- Fe)	3D supramolecular Fe-chloranilate (CAN) frameworks containing *x*+y waters per formula unit $[Fe_2(CAN)_3(H_2O)_x]\cdot yH_2O$ for {*x*,y} = {0,0; 4,0; and 4,4}	300	--	--	confirmed that all three phases contain high spin Fe^{3+} only	25D003
Rh(IS/α-Fe)	catalyst of Fe/C with commercial amorphous carbon produced by Norit company	300	--	--	identified the major doublet assigned to amorphous carbon, and alpha-Fe, and spm-Fe_2O_3	25Z002
Rh(IS/α-Fe)	composite of $Ti_3C_2/In_2S_3/CoFe_2O_4$	300	--	--	identified two sextets assigned to Fe^{3+} in tetrahedral and octahedral sites and a doublet of HS Fe^{2+} in tetrahedral sites	25X001
xx	compounds having several Fe sites with overlapping components	v	--	--	developed a program to fit a spectrum having different widths of resonant lines assuming this shape to result from multidimensional Gaussian distribution	25Y004
Rh(IS/α-Fe)	narrowly sieved iron particles with a mean diameter of 49 μm in the progress if oxidation in laminar flow reactor	300	--	--	determined the bulk composition of the quenched particles with respect to *α*-Fe and its three oxides FeO, Fe_3O_4, and Fe_2O_3 as the function of extraction position at 25, 28, 33, 38, 43, 48, 88, 137 and 186mm of the height above burner	25S001
Rh(IS/α-Fe)	NbC-Fe and NbC-FeNi milled powders, and in NbC-Fe and NbC-Fe-Mo_2C cermets, and NbC-FeNi and NbC-FeNi-Mo_2C cermets	v	--	--	observed magnetic sextets in both NbC-Fe and NbC-FeNi milled powders and in NbC-Fe and NbC-Fe-Mo_2C cermets with B_{hf} of 29.4 T to 33.1 T, however, B_{hf}=0 for NbC-FeNi and NbC-FeNi-Mo_2C cermets with gamma-FeNi phase	25P003
Fe-57 14.40 keV Transition: Organic Compounds						
Rh(IS/α-Fe)	(EmL)Fe(N_3) (Em: 1,1,7,7-tetraethyl-1,2,3,5,6,7-hexahydro-3,3,5,5-tetramethyl-s-indacene)	90	0.72	0.55	identified three-coordinate three-coordinate, high-spin, terminal, azido, Fe(II)	25O001
Rh(IS/α-Fe)	(EmL)FeCl (Em: 1,1,7,7-tetraethyl-1,2,3,5,6,7-hexahydro-3,3,5,5-tetramethyl-s-indacene)	90	0.74	0.30	identified three-coordinate HS Fe^{II} (coordinated by Cl and 2N)	25O001
Rh(IS/α- Fe)	3D supramolecular Fe-chloranilate (CAN) frameworks containing *x*+y waters per formula unit $[Fe_2(CAN)_3(H_2O)_x]\cdot yH_2O$ for {*x*,y} = {0,0; 4,0; and 4,4}	300	--	--	confirmed that all three phases contain high spin Fe^{3+} only	25D003
Rh(IS/α-Fe)	bacterial cytochrome c peroxidase from Nitrosomonas europaea (Ne bCcP) before and after reaction with H_2O_2	4	--	--	identified 3 species of 6-coordinate Fe^{II} (S=0) or Fe^{III} (S=1/2) in E and P hemes with the ratio of total E (Fe^{II}+Fe^{III}) to P of 62/38 before H_2O_2-reaction, and S=1/2 Fe^{III} species in E and P hemes, compound 2 and compound 1 in amounts relative to total iron of 56%, 16%, 7%, 11% after reaction	25H006
xx(IS/α-Fe)	choerospondias axillaris polysaccharide-iron (III) complex	298	0.34	0.80	determined the IS and QS of octa-Fe(III) similar to other polysaccharide-iron (III) complexes known to possess a β-FeOOH structure	25X002
Rh(IS/α- Fe)	clusters of $NiFe_4S_4$ and $Ni_2Fe_3S_4$ (in [Na(15-crown-5)·Et_2O][IMesNi$Fe_4S_4(N(SiMe_3)_2)_4$], and in $Na(THF)_2(IPrNi)_2((Me_3Si)_2NFe)_2FeS_4$)	80	--	--	revealed that Fe oxidation states in $NiFe_4S_4$ are $Fe^{2.5+}$(4 species) and that $Ni_2Fe_3S_4$ have one Fe^{3+} and two Fe^{2+}	24F019
Rh(IS/α-Fe)	$CoFe_2O_4$ synthesized using Ginkgo Biloba leaves, flax seeds, tomato juice, and persimmon fruit	300	--	--	determined the cation distribution and ratio of magnetically-split and spm-doublet fractions	25T003
xx	diiron complexes of tetradentate ligands with different flanking donors $C_{44}H_{48}Fe_2N_{8*1.5}C_6H_6$ and $C_{40}H_{36}Fe_2N_4S$	4	--	--	identified two doublets mainly (85%) assigned to HS Fe(II)	24S081
Rh(IS/α- Fe)	dinitrosyl iron complex Fe(PhNHPDI)$(CO)_2$	300	-0.083	1.337	identified S=0 Fe(II) center with a doubly reduced PhNHPDI ligand	25F001
Rh(IS/α- Fe)	dinitrosyl iron complex Fe(PhNHPDI)Cl_2	300	0.886	2.00	identified S=2 Fe(II) center with a neutral PhNHPDI ligand	25F001

Source	Absorber	Temp	IS	QS	Comments	Code
Rh(IS/α-Fe)	dinuclear complex of [(calix[4]arene)$_2$-Fe^{III} $_2$ (μ^2-OMe)$_2$]·2MeOH, bearing two distally disposed salicylideneamine binding sites	v	--	--	identified mainly two HS doublets, and the appearance of the minor third LS doublet was caused by inclusion of MeOH molecule within the calix[4]arene macrocyclic cavity	25S006
Rh(IS/α- Fe)	Fe(IV) complex supported by bisamide ligands FeDipp2	80	0.00	2.70	identified S=1 4-coordinate Fe(IV) complex	24Z033
Rh(IS/α- Fe)	Fe(IV) complex supported by bisamide ligands FeMes2	80	-0.15	3.00	identified S=1 4-coordinate Fe(IV) complex	24Z033
Rh(IS/α-Fe)	Fe-containing proteins, supramolecular structures, microbial cells/tissues and biomedical reagents	v	--	--	reviewed Mössbauer spectroscopy basics and contributions to biomedical sciences	25H007
Rh(IS/α- Fe)	Fe/ZIF-8 calcined at 900 ◦C for 3 h in an argon atmosphere without and with Vitamin C	300	--	--	identified species Fe^{II}-N$_4$, O$_x$-Fe^{III}-N$_4$, and phases of iron oxides, α-Fe and Fe$_3$C	21H029
Rh(IS/α-Fe)	FeBTC (Fe(III)-benzene 1,4,5-tricarbonate)	300	--	--	reviewed the Mössbauer spectra of FeBTC and MOF MIL-100(Fe) built of Fe and BTC and calculated the Mössbauer spectra for the model structures	25R004
Rh(IS/α-Fe)	Fe^{II}(BPA^{Me2}S)Br frozen in THF	80	0.93	3.29	identified HS Fe(II) in coordination 5 (Br, S and 3N)	25Y002
Rh(IS/α-Fe)	hexakis(urea-O)iron(III) nitrate	90	0.511	0	identified Fe^{3+} coordinated by six urea ligands	25B005
Rh(IS/α- Fe)	metal-organic framework after adsorption of the pyrrole molecules, {Fe(pz)[Ni-(CN)$_4$]}⊃Py^t (1⊃Py^t)	v	--	--	identified a doublet of HS Fe(II) at 300 K and two doublets at 80 K, assigned to LS Fe(II and HS Fe(II) and observed that the spin transition occurs, ranging from ca.300 to 250 K	25L008
Rh(IS/α-Fe)	model compounds enclosing the [2Fe–2S] cores	v	--	--	reviewed the isomer shift and quadrupole splitting exhibiting different iron oxidation states such as [2Fe–2S]$^{2+}$ ([Fe^{III}-Fe^{III}]) and the mixed-valent form [2Fe–2S]$^{1+}$ ([Fe^{III}-Fe^{II}]) and [2Fe–2S]^0 ([Fe^{II}-Fe^{II}])	25Y001
Rh(IS/α-Fe)	oxo-bridged trinuclear complex [Fe$_3$O(piv)$_6$(py)$_3$] (piv=pivalate, py=pyridine)	300	--	--	identified mixed-valence doublets characteristic of Fe$^{2.5+}$ and a doublet of Fe^{3+} above the trapping-detrapping crystallographic transition and the doublets of Fe^{2+} and Fe^{3+} below the transition (around 120 K)	25X003
Rh(IS/α-Fe)	periplasmic heme-c enzyme cis-trans isomerase purified from Pseudomonas aeruginosa (Pa-cti)	77	0.46	1.22	confirmed the presence of an octahedral low-spin ferrous iron (Fe^{II}, S=0)	25M002
Rh(IS/α-Fe)	products from the reactions of dimethylarsenate incorporated into ferrihydrite with 1 mM Fe(II) at pH 4 and 7	6.2	--	--	revealed after reaction that 52.0–53% of the ferrihydrite in the coprecipitate is transformed to lepidocrocite	25C006
Rh(IS/α-Fe)	radioactive waste without and with BN in various proportions	300	--	--	identified the doublets of Fe^{2+} and Fe^{3+} and determined the ratio Fe^{3+}/Fe(total) decreasing from 1.00 to 0.76 to 0.67 and to 0.45, as the mass proportion of BN added to make the glass increased from 0 to BN$_{0.25}$, BN$_{0.5}$, and BN$_{0.75}$ in feeds	25R003
Rh(IS/α-Fe)	reduced and spent Fe foam catalysts promoted with Na or K or Rb or Cs nitrate impregnation	300	--	--	identified magnetic phases of χ-Fe$_5$C$_2$, Fe$_3$C, α-Fe, and doublets Fe^{2+}(spm), Fe^{3+}(spm)	25A007
Rh(IS/α-Fe)	trielyl-derived complex (K_2(18-crown-6)$_2$Cp][(NON) InFe(CO)$_4$] (NON=4,5-bis(2,6-diisopropyla nilido)-2,7-di-tert-butyl-9,9-dim ethylxanthene, E=Al, Ga, In)	80	-0.08	1.97	revealed an increased perturbation of the iron electric field gradient as group 13 is descended, consistent with interactions with increasingly large ligand donor atoms	25G006
Rh(IS/α-Fe)	trielyl-derived complex [K(18-crown-6)][(NON)AlFe (CO)$_5$] (NON=4,5-bis(2,6-diisopropyla nilido)-2,7-di-tert-butyl-9,9-dim ethylxanthene, E=Al, Ga, In)	80	-0.24	1.08	revealed an increased perturbation of the iron centred electric field gradient as group 13 is descended, consistent with interactions with increasingly large ligand donor atoms	25G006
Rh(IS/α-Fe)	trielyl-derived complex [K(18-crown-6)][(NON)GaFe (CO)$_5$] (NON=4,5-bis(2,6-diisopropyla nilido)-2,7-di-tert-butyl-9,9-dim ethylxanthene, E=Al, Ga, In)	80	-0.13	1.53	revealed an increased perturbation of the iron centred electric field gradient as group 13 is descended, consistent with interactions with increasingly large ligand donor atoms	25G006

Source	Absorber	Temp	IS	QS	Comments	Code
Rh(IS/α-Fe)	water-soluble μ-S nitrosyl iron complex with acetylcysteine $[Fe_2(C_5H_8NO_3S)_2(NO)_4]\cdot 2H_2O$	295	0.0872	1.0407	identified a unusually sharp doublet from the low-spin state of d^6/d^7 dimer delocalized on Mössbauer timescale, but showing an S=1/2 EPR signal	25R002
Rh(IS/α-Fe)	$[Co^{III}(O)^{57}Fe^{III}poat]^+$ (where tripodal ligand $[poat]^{3-}$=(N,N′,N″-[nitrilotris(ethane-2,1diyl)]tris(P,P-diphenyl phosphinic amido))	4	--	--	identified spin values S(Co), S(Fe) S(tot) equal to 3/2, 5/2 and 1, respectively	25P002
Rh(IS/α-Fe)	$[Fe(3\text{-}bpp)_2](psca)_2$ $2.5H_2O$	v	--	--	main doublet is Fe(II)LS, both at 78 and 298 K; the second doublet area increases from 15 to 22 % as temperature increases from 78 to 298K	25K011
Rh(IS/α-Fe)	$[Fe(Ph\text{-}BIAN)_3](BPh_4)_2$ with alpha-diimine ligand bis((phenyl)imino) acenaphthene (Ph-BIAN)	v	--	--	confirmed that the complex has a LS-Fe^{III}-$(L^{c-})(L^0)_2$ ground state and undergoes an overall valence-tautomeric interconversion to HS-Fe^{II}-$(L^0)_3$	25J003
Rh(IS/α-Fe)	β-hematin synthesized in aqueous-acetate medium and aqueous-only medium	v	--	--	identified the rates of spin-spin relaxation using Blume model and explained the increased spectral asymmetry for the aqueous-only medium synthesis	25H005
<u>Fe-57 14.40 keV Transition: Terrestrial and Extraterrestrial Minerals</u>						
Rh(IS/α-Fe)	black volcanic ashes of the tephri–phonolite'Pozzolane Nere' magma from the Colli Albani (Rome, Italy)	300	--	--	identified three paramagnetic components attributed to Fe^{2+} and Fe^{3+} glass sites and determined the relative Fe^{2+} and Fe^{3+} fractions	25F002
xx	coal mine drainage sludge	300	--	--	identified two doublets, both assigned to Fe(III)	25C008
Rh(IS/α- Fe)	composition $MgSiO_3$ +$FeAlO_3$ (60: 40) before and after grain growth at 2000 K and 27 GPa	300	0.421	1.015	observed the increase of IS up to 0.434 mm/s and decrease in QS to 0.988 mm/s and no detectable ferrous iron	24F018
Rh(IS/α-Fe)	German bentonite clay and Italian red modified montmorillonite clay	300	--	--	identified mainly hematite in German clay and minor illite/kaolinite phase, and main kaolinite/illite in Italian clay	25N001
Rh(IS/α-Fe)	iron ore from the Wugang and Hengyang BIFs in China	300	--	--	identified hematite and maghemite phases in different proportions	25K012
Rh(IS/α- Fe)	phosphosilicate wastes produced by adding a borosilicate frit	300	--	--	found evidence of hematite formation for very small (2.5 and 3%) frit addition, but observed that the hematite formation was suppressed with the additions of 5 wt % –15 wt % borosilicate frit	25E003
Rh(IS/α-Fe)	photo-electrochemically (PEC)-synthesized and H_2O_2-produced acid mine drainage precipitates	300	--	--	identified doublets characteristic of schwertmannite	25W002
Rh(IS/α-Fe)	radioactive waste without and with BN in various proportions	300	--	--	identified the doublets of Fe^{2+} and Fe^{3+} and determined the ratio Fe^{3+}/Fe(total) decreasing from 1.00 to 0.76 to 0.67 and to 0.45, as the mass proportion of BN added to make the glass increased from 0 to $BN_{0.25}$, $BN_{0.5}$, and $BN_{0.75}$ in feeds	25R003
<u>Sb-121 37.20 keV Transition</u>						
$BaSnO_3$(IS/InSb)	bulk $Sb_{0.10}Se_{0.90}$ and $Sb_{0.15}Se_{0.85}$ glasses	4.2	--	--	found the electric-quadrupole splitting is in the range $9 \le eQV_{zz} \le 11$ mm s^{-1}, and the average value of the asymmetry parameter $\eta=(V_{xx}-V_{yy})/V_{zz}=0.8 \pm 0.1$	25K010
<u>Sn-119 23.80 keV Transition: Inorganic Oxides</u>						
$CaSnO_3$, T = 78 K	$SnAlBO_4$ and $SnGaBO_4$	v	--	--	fitting the spectra collected at 298 K is good with 1 doublet, however, fitting the spectra collected at 78 K requires two doublets, both in the range of Sn(II) isomer shift; this is explained by structural modulation	25W004
<u>Sn-119 23.80 keV Transition: Metals and Alloys</u>						
xx	alloy $Ge_{12}Sb_8Sn_4Te_{28}$	300	3.28	0.31	calculated isomer shift and quadrupole splitting distributions Sn/Te sites considering different distributions of Sn, Sb and Ge vacancies in the Ge sublattices	25G007
<u>Sn-119 23.80 keV Transition: Miscellaneous Inorganic Compounds</u>						
xx	γ-Sn_3N_4 prepared at 325 °C via the Mg_3N_2 route	300	--	--	observed two Sn(IV) singlets with the isomer shifts of 1.12 and 0.64 mm/s and the spinel ratio (2:1) assigned larger one to the octahedral $Sn_2@N_6$ site and the smaller one to tetrahedral $Sn_1@N_4$	25Z001

Actinides:
25F001 25H005 25J003 25K012 25R002

Analysis:
25H005 25Y004

Anti-ferromagnetism:
24S081 24S082 25A004 25F003 25M001 25M003 25N003 25P004 25R001 25S002 25W007 25Y002

Applied Electric Field:
20V020 21H029 25C006 25D003 25F001 25J003 25L008 25M002 25P001 25T002 25W002 25W006 25X001 25Z003

Applied Magnetic Field:
24E008 24F019 24S081 25G008 25H006 25H007 25P004 25X003

Asymmetry Parameter:
25G007 25H007

Bacteria:
24F019 25A006 25H006 25H007 25M002 25X002

Biological Applications:
21A044 24F019 25A006 25C005 25H005 25H006 25H007 25K013 25M002 25T003 25X002 25Y001

Carbonyl Complexes:
25B008 25C008 25G006 25R003 25R004 25W005

Catalysts:
20V020 21H029 24F019 25A007 25L007 25L009 25M002 25O001 25S005 25T001 25W001 25W005 25Y003 25Z002 25Z003

Charge States:
21H029 25A007 25D003 25F003 25J003 25L009 25W001 25W005 25Y003

Charge Transfer:
21H029 24F018 25A007 25B008 25C005 25C006 25D003 25F003 25H006 25J003 25L009 25M002 25S005 25T002 25W005 25W006 25X003 25Y003 25Z002 25Z003

Chemical Identification:
20V020 21A044 21H029 24E008 24E009 24F018 24F019 25A007 25B005 25B006 25B007 25C005 25C007 25D003 25D004 25E002 25E003 25F003 25F004 25G006 25H005 25H009 25J003 25J004 25K012 25K014 25L008 25L009 25P003 25R003 25S001 25W001 25W003 25W005 25Y001 25Y003 25Z002

Chemical Kinetics:
25A006 25C006 25L007 25T001 25T003 25W001 25W002 25W005 25X002

Chemical Reactions:
21H029 25A006 25A007 25B008 25C005 25C006 25C007 25C008 25D004 25E002 25E003 25H006 25H007 25H009 25K012 25L007 25L009 25M002 25R002 25S001 25S005 25S006 25T002 25T003 25W001 25W002 25W004 25W005 25X002 25Y001 25Y003 25Z001 25Z002 25Z003

Clay Minerals:
25N001

Coal:
25C008

Computer Programs:
25G007 25H005 25Y004

Conversion Electron Spectroscopy:
24O011 25A005 25L006 25P003 25S004

Crystal Defects:
20S095 24F018 25G007 25K010 25P004

Crystal Field Theory:
25J003 25L007 25W001 25W006 25Y001

Curie Temperature:
25N003

Debye Temperature:
25F003 25W004 25X003

Decomposition:
25A007 25H008 25H009 25S005 25T001 25T003 25W004 25X002 25X003

Depth Selection:
24O011 25L006 25S004

Diffusion:
25L008 25S001

Distributions of Magnetic Fields:
20S095 21A044 24E008 25A004 25C005 25C006 25E002 25F003 25G008 25H006 25H008 25J004 25K012 25L006 25L007 25M003 25P004 25S003 25S004 25S005 25T001 25W003 25W005 25W007 25Y004 25Z002 25Z003

Electron Diffraction:
20V020 21H029 25B007 25D003 25G008 25H009 25L006 25X001

Electron Hopping:
25X003

Electron Microscopy:
20V020 21A044 21H029 24O011 25A004 25A007 25B007 25C005 25C006 25C008 25D003 25E003 25F003 25F004 25G008 25H005 25H009 25J004 25K012 25K013 25K014 25L006 25M001 25N001 25N002 25N003 25P001 25P003 25S001 25S003 25T001 25T002 25T003 25W003 25W006 25W007 25X001 25Y003 25Z001 25Z002 25Z003

Electron Paramagnetic Resonance:
21H029 24F019 24Z033 25B008 25H006 25H007 25L007 25P002 25P004 25R002 25S004 25W001 25Y003

Electronic Spectroscopy:
21A044 21H029 24S081 25A004 25A007 25B006 25B007 25C005 25C006 25F001 25F002 25F003 25H005 25H006 25H007 25J003 25K010 25K014 25L009 25M002 25N002 25P001 25P002 25R002 25S004 25S005 25T001 25T003 25W001 25W002 25W005 25W006 25X001 25X002 25Y002 25Y003 25Z001 25Z002 25Z003

Ferromagnetic Materials:
25A005 25J004 25N003 25P004 25S004 25Y002

Frozen Solutions:
24F019 25B008 25H006 25H007 25Y002

Glass Transition:
25F002 25K010 25R003

Glasses and Amorphous Substances:
25E003 25F002 25K010 25R003

Glazes:
25D004

Hartree-Fock Calculations:
24S081 24Z033 25B008 25G006 25G007 25K010 25R002 25R004 25W006 25X003 25Y001 25Y002 25Z003

Hemoglobin:
25H005 25H006 25H007

High Magnetic Field Measurements:
25X003

High Pressure Experiments:
24F018 25C007

Inorganic Cyanides:
25L008

Instrumentation:
25S001 25Z001

Irradiation Experiments:
25K010 25R003

Kinetics:
21H029 24F018 25A006 25C006 25C007 25G008 25H006 25H008 25L007 25T001 25T003 25W001 25W002 25W005 25X002 25Y003

Laser Annealing:
25K010 25K013

Lattice Dynamics:
24Z033 25C006 25G006 25P001 25S002 25W004

Layer Compound:
25L008 25N001 25N002 25N003 25S001 25W006

Mass Spectroscopy:
21H029 25Y002

Mechanical Milling:
25G008 25S003

Metals and Alloys:
20S095 24E008 24O011 25A005 25C005 25G007 25G008 25H008 25H009 25J004 25K010 25L009 25P003 25R001 25S001 25S003 25S004 25T002

Molecular Orbital Calculations:
24Z033 25G006 25R004

Morin Temperature Measurements:
25F003

Multilayered Films:
25A005 25X001

Myoglobin:
25H005 25H006 25H007

Nanocrystal:
21A044 24O011 25A006 25B006 25C005 25C008 25E002 25G008 25H008 25K013 25K014 25L007 25N002 25P004

Neel Temperature:
24S082 25F003 25R001 25S002 25W007

Neutron Diffraction:
25D004

Nuclear Magnetic Resonance Experiments:
24F019 24Z033 25B008 25F001 25K013 25M002 25O001 25R003

Phase Transitions:
25K010 25L008 25M003 25N003 25R001 25S002 25W006 25X003

25Z003

Polymers:
25R002 25R004

Quantitative Analysis:
24S081 25F001 25H006 25H007
25K012 25P002

Raman Spectroscopy:
24E009 25B006 25B008 25D003
25D004 25E003 25F002 25K010
25M002 25P001 25W004 25W005

Rare Earths:
24E009 24F019 24Z033 25F003
25F004 25K012 25R001 25S002
25W007 25Y001 25Z003

Relaxation:
20V020 25A007 25B007 25C005
25C008 25E002 25F003 25F004
25H005 25J004 25K012 25K013
25K014 25L007 25M001 25M003
25T001 25Z002

Reviews:
20S095 25C007 25Y001

Scattering Experiments:
25R001

Second Order Doppler Shift:
25F003 25S002

Semiconductors:
21A044 25B006 25B007 25K010
25T003

Single Crystal Experiments:
24Z033 25K011 25L006 25O001
25R001 25R002 25X003 25Y002

Speromagnetic-type order:
25L007

Spin Crossover:
25K011 25L008 25X003

Steel:
24O011

Strain Effects:
20S095 21A044 25S003

Superparamagnetism:
20V020 25A007 25B007 25C005
25C008 25E002 25F004 25H005
25J004 25K012 25K013 25K014
25L007 25M001 25T001 25Z002

Surface Studies:
20V020 21H029 25A006 25C005
25K014 25L008 25S001 25X001

Synchrotron Radiation:
25K010

Terrestrial and Extrater. Minerals:
24F018 25C008 25E003 25F002
25K012 25N001 25R003 25W002

Texture:
24E008 25H009 25L006 25L007
25N001 25N002 25N003 25S001
25S005 25W006

Theory:
25G007 25H007 25R004 25Y004

Thin Films:
24O011 25A005 25L006 25S004

Variable Thickness:
25L006

Volcanic Materials:
25F002

X-ray Diffraction-Powder:
20S095 20V020 21A044 21H029
24E008 24E009 24F018 24O011
25A004 25A005 25A006 25A007
25B005 25B006 25C005 25C006
25C007 25C008 25D003 25D004
25E002 25F002 25F003 25F004
25G007 25G008 25H005 25H008
25H009 25J003 25J004 25K010
25K012 25K013 25K014 25L006
25L008 25L009 25M001 25N002
25P001 25P004 25R002 25R003
25S002 25S003 25T001 25T003
25W001 25W002 25W003 25W004
25W005 25W006 25W007 25X002
25Y001 25Z001 25Z002 25Z003

X-ray Diffraction-Single Crystal:
24S081 24Z033 25F001 25G006
25H005 25K011 25N003 25O001
25P002 25R001 25R002 25X003
25Y002

ABBREVIATION LISTING

--	multiple components
IS/	isomer shift relative to
v	variable
xx	material not reported

ISOTOPE INDEX

Eu-151: 25R001

Sb-121: 25K010

Sn-119: 25G007 25W004 25Z001

MÖSSBAUER SPECTROSCOPY
NEWSLETTER

April 2025

MEDC Interview, Nov. 2024

Prof. Tadeusz Szumiata was visiting Prof. Yann Garcia at University catholique de Louvain (UCLouvain), Belgium. MEDC asked him a few questions on this special occasion.

MEDC: Prof. Tadeusz Szumiata, Greetings. You were visiting Prof. Yann Garcia at UCLouvain. What was the initial purpose of your visit?

TS: Well, initially, I planned to spend two weeks at UCLouvain, but I received an invitation from the European Association of National Metrology Institutes - EURAMET (https://www.euramet.org/) to review research projects submitted under the European Partnership on Metrology (https://www.metpart.eu/). Very conveniently, the reviewers' meeting was scheduled exactly in Louvain-la-Neuve (LLN) just one week before.

MEDC: How were received your lectures?

TS: Very positively I must say. I was very glad and honoured at the same time to give lectures for the staff and students of UCLouvain. I noticed a great interest and understanding of the subject presented. I tried to explain in simple words the application of Mössbauer spectrometry in environmental surveillance as well as in quality control in metallurgical industry. I also presented new perspectives in metrology after the redefinition of mass standard and the entire SI system of units.

MEDC: Overall, what is your first impression of UCLouvain and its facilities?

TS: Very positive. It is perfect place for teaching students and make research in many modern domains of science. I know, that especially the school of chemistry at UCLouvain is very famous all over the word. Owing to excellent equipment and generations of very experienced staff of chemists, UCLouvain achieves many successes, and is considered as the leading institution among French speaking universities of the country.

MEDC: Do you plan to collaborate further with UCLouvain and Prof. Garcia, in

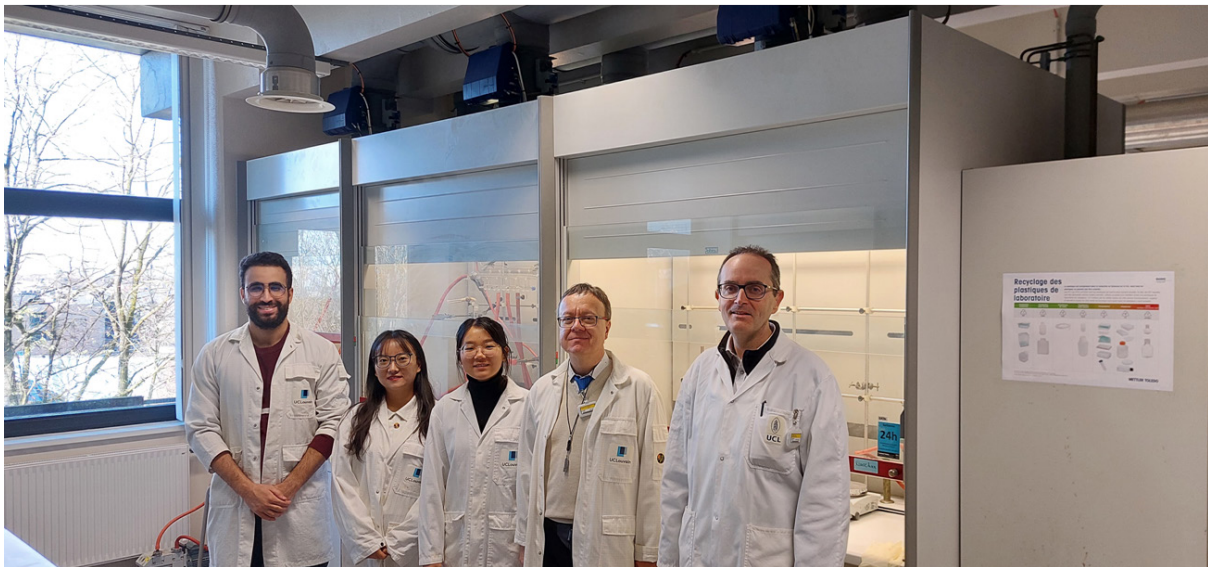

L-R: Group photo in the laboratory with Dr. Youssef Draoui, Xiaochun Li, Dr. Mengmeng Wang, Prof. Tadeusz Szumiata and Prof. Yann Garcia

particular?

TS: Of course. First of all, I would like to express my gratitude to Prof. Yann Garcia for inviting me to UCLouvain and for previous cooperation as well as for the real friendship. Most likely future cooperation will be focused on temperature-evoked spin transition phenomena investigations in organometallic compounds by means of Mössbauer spectrometry, but not only.

MEDC: What do you mean?

TS: I mean regarding the use of developed balances in Radom that could be applied to nanochemistry issues.

MEDC: That sounds interesting. But, could you please tell us more about your own research. We heard about your recent success in environmental science applied Mössbauer spectroscopy and metrology.

TS: Since for about ten years, I have had great satisfaction in applying Mössbauer spectrometry to the investigation of various types of environmental samples like fly ashes from powerplants, soils, street dust and airborne particulate matter. I combine this technique with other methods – mostly with magnetometry and chemical analysis. It requires intensive cooperation with numerous research groups at my home university (Casimir Pulaski Radom University, Poland), as well as other scientific institutions in Poland and in the world. Being a physicist, I also try to help my colleagues-engineers in quality control of steel elements by means of Mössbauer spectrometry. My second domain of activity is modern mass metrology. I keep close links with the metrological industry and national metrological institutes. I was very proud to be in 2018, the first technical delegate of Poland to Sèvres (Le Bureau international des poids et mesures, BIPM) in order to explore the new standard of mass (so-called Watt-Kibble Balance). It opened many perspectives.

MEDC: Regarding instrumentation, we also heard that you will equip your laboratory with new modern Mössbauer instruments. Was the choice of the type of instruments difficult?

TS: That is true. We were successful with the application to the Polish Ministry of Science and High Education for the equipment grant. One of the crucial items of new equipment will be a set of Mössbauer spectrometers. Indeed, the choice is not easy, because fewer and fewer companies have decided to manufacture Mössbauer due to narrow market niche. Moreover, there is a strong discussion among the Mössbauer community, how to facilitate and automate the work with this technique but at the same time not to limit the hardware flexibility. And finally, due to the complicated geopolitical situation, this requires a serious storm-brain within leading Mössbauer spectrometry organizations, most probably at the IBAME level too.

MEDC: Talking about IBAME, who are the polish representatives at IBAME? We heard that the polish Mössbauer society undertook some changes. Could you please inform us?

TS: I would call it a good continuation. Poland has two IBAME representatives: Prof. Krzysztof Szymański and also Prof. Elżbieta Jartych, who was recently reelected with the great majority of votes. Prof. Jartych is a General Chair of the ICAME2025 conference.

MEDC: As we all know, ICAME25 will be organized in Gdansk, a beautiful city bordered by the Baltic sea, but we noticed that no Mössbauer groups are located in this city. Could you please explain us this choice?

TS: Mössbauer spectrometry is a very popular method in Poland and is present in several cities. The Organizers of ICAME25 do not intend to favor any of them, that is why the Committee has chosen Gdansk. But of course, it is not the only reason. Gdansk is a beautiful, Hansatian city located at the Baltic Sea coast. Gdansk is distinguished by its multiculturalism and rich history. It is a strong academic centre as well as a symbol of the Polish fight for freedom. You are very welcome to attend ICAME25 and to visit Gdansk.

MEDC: Thank you very much Prof. Szumiata. We wish you a safe trip back to Radom.

TS: You are very welcome, thank you.

Development of Fe^{II} Tetranuclear Cages: Spin Crossover and Their Ammonia Sensing Application

Weiyang Li, Yann Garcia (✉)
Institute of Condensed Matter and Nanosciences, Molecular Chemistry, Materials and Catalysis (IMCN/MOST), Université catholique de Louvain, Place Louis Pasteur 1, 1348 Louvain-la-Neuve, Belgium
Email: yann.garcia@uclouvain.be

Bibliography

Dr. Weiyang Li was born in Wuchang (P. R. China) in 1994. He received his M.Sc degree in Materials Physics and Chemistry from Shanghai University of Engineering Science in 2019. During 2019-2023, he was pursuing his Ph.D. under the supervision of Prof. Yann Garcia at UCLouvain, where he was introduced to experimental ^{57}Fe Mössbauer spectroscopy. His research interests encompass the design, synthesis, characterization, and application exploration of Fe^{II}-based spin crossover tetranuclear cages. Back to China, he is now seeking for new challenges.

Prof. Dr. Yann Garcia was born in Castres, France in 1972. He obtained his doctorate in material science and solid state chemistry from the Univ. of Bordeaux at the ICMCB-CNRS under the supervision of Prof. Olivier Kahn in Jan. 1999. He then joined the Institute of Inorganic and Analytical Chemistry of the Univ. of Mainz (Germany) in Feb. 1999 to work with Prof. Dr. Philipp Gütlich as a TMR EU post-doctoral fellow until 2001. While he got a CNRS permanent position (Sorbonne Univ.), he accepted the offer of UCLouvain to work as assistant prof. in analytical chemistry. He was subsequently appointed as associate Prof. in 2004, Professor in 2009 and elected as head of the Molecular Chemistry, materials and catalysis division of the IMCN institute in 2023. The research interests of Prof. Garcia extend from photoswitchable coordination compounds, spin crossover materials to smart sensors, medicinal and environmental applications, where Mössbauer spectroscopy is considered as a key tool. His laboratories gather several spectrometers operating in transmission mode. Prof. Garcia has published more than 300 publications with several cover pages of top chemistry journals and book chapters. Among his editorial activities, Prof. Garcia is associate editor of the Mössbauer Effect Reference Data Journal and edited together with Prof. J. Wang (MEDC, DICP) and Prof. Zhang (MEDC, DICP) a book on Mössbauer spectroscopy focused on chemistry and its applications (Wiley VCH, 2024). Prof. Garcia is president of the French Speaking Mössbauer Society (GFSM, www.gfsm.fr) and IBAME vice chair (www.ibame.org).

Table of Contents:

I. Introduction and context
II. 1. First SCO $Fe^{II}_4L_6$ cage based on pyridyl-hydrazone sites
III. 2. SCO in a family of $Fe^{II}_4L_6$ cages with pyridyl-hydrazone ligand scaffolds modulated by solvents, counter anions and substituents
IV. 3. From a mononuclear $Fe^{II}L_2$ complex to a SCO $Fe^{II}_4L_6$ cage for colorimetric ammonia sensing
V. 4. A SCO $Fe^{II}_4L_4$ cage for fast ammonia sensing and the monitoring pork spoilage
VI. General conclusions
VII. Acknowledgments
VIII. References

The 4802 issue mainly published the parts of the first section **Introduction and context**, the second section **1. First SCO $Fe^{II}_4L_6$ cage based on pyridyl-hydrazone sites and** the third section **2. SCO in a family of $Fe^{II}_4L_6$ cages with pyridyl-hydrazone ligand scaffolds modulated by solvents, counter anions and substituents**. In the 4801 issue, we also added the photograph and biography of authors.

Introduction and context

Spin crossover (SCO) phenomenon in transition metal complexes with $3d^4$-$3d^7$ electronic configurations is regarded as an appealing field of investigation due to its potential applications in memory devices, nano-electronics/spintronics and sensors [1-3]. Such outstanding physical properties are caused by the reversible switching between high-spin (HS) configuration and low-spin (LS) configuration driven by external perturbations such as variations in temperature, pressure, electric field, light irradiation and guest molecules [1-3]. To date, the most widely reported SCO compounds in the literature are those containing Fe^{II} ions, which are accompanied by dramatic changes in magnetic, structural and optical properties [4]. Among Fe^{II} SCO complexes, mononuclear compounds with FeN_6 octahedral coordination geometry have been intensively studied and molecular design approaches are well-established [1]. In contrast, the study in polynuclear SCO Fe^{II} systems is still in its relative infancy [1, 5, 6].

Polynuclear Fe^{II} SCO systems with multiple active centers have been reported in binuclear, trinuclear, tetranuclear, pentanuclear, hexanuclear, and even octanuclear systems, with the configuration shown in **Scheme 1** [7]. In particular, tetranuclear tetrahedral molecular cages have attracted a great deal of interest because of the presence of well-defined central cavities, which offer the possibility of altering the SCO behavior via host–guest interaction [7]. Also, the specific recognition of guest molecules due to size effects or steric hindrance in the cavity could induce changes in spin states as well as optical properties, which may turn the SCO cages into colorimetric sensors [8]. In addition, the usual requirements for molecular storage devices involve the need for two or more stable spin states, while Fe^{II} SCO cage compounds theoretically have accessibility up to five spin states, *i.e.*, $(Fe^{II}LS)_n(Fe^{II}HS)_{4-n}$ (n = 0–4) [9]. So far, only 17 tetranuclear tetrahedral cages have been reported to have SCO activity in the solid-states, and all SCO cages used imidazole-imine (16 cases) and thiazole-imine (1 case) coordination sites [10-18]. Meanwhile, due to the limited number of solid Fe^{II} SCO cages reported in the literature (9 in total) [10-18], studies on their functionality have been scarce and limited to adsorption of guest molecules (I_2[15] and C_{60}[16]) as porous adsorbents. Given the importance of ligand design and versatility for SCO cages, the development of new coordination sites with unusual molecular structures as well as new applications is significant for the field.

Ammonia (NH_3) is widely used in agriculture, industry, medicine and so on [19]. However, even low concentrations of $NH_{3(g)}$ can impair the human immune system and cause serious medical issues. In addition, $NH_{3(g)}$ as an important component of total volatile basic nitrogen can be a potential indicator of the decomposition for high-protein foods, and therefore can be used as a tracker for food safety [20]. Hence, research on high-performance $NH_{3(g)}$ sensor materials and easy to operate, timely, and low-cost analytical methods is highly needed nowadays for human health. Fe^{II} based coordination complexes have emerged as promising molecular sensing materials, because the coordination environment of the metal centre is sensitive to subtle changes triggered by guest molecule intercalation [21]. Meanwhile, optical outputs are altered by the spin state transition [22]. Our group reported three mononuclear HS complexes, $[Fe^{II}(trz\text{-}tet)_2(H_2O)_4]\bullet nH_2O$ (trz-tetH = 5-(4*H*-1,2,4-triazol-yl)-2*H*-tetrazole), $[Fe(Hbta)_2(H_2O)_2]\bullet 2H_2O$ (H_2bta = bis(1*H*-tetrazol-5-yl)amine) and $[Fe^{II}(H_2btm)_2(H_2O)_2]Cl_2$ (H_2btm = di(1*H*-tetrazol-5-yl)methane) as colorimetric sensors for various volatile organic compounds including $NH_{3(g)}$ under ambient conditions [23-27]. On this basis, considering the size effect of the cavities in tetrahedral cages may lead to selective recognition of guest molecules, which in turn leads to changes in spin states and optical properties, giving the Fe^{II} SCO cage potential as a colorimetric sensor.

There are two main objectives in Weiyang Li's thesis [28].The first is to

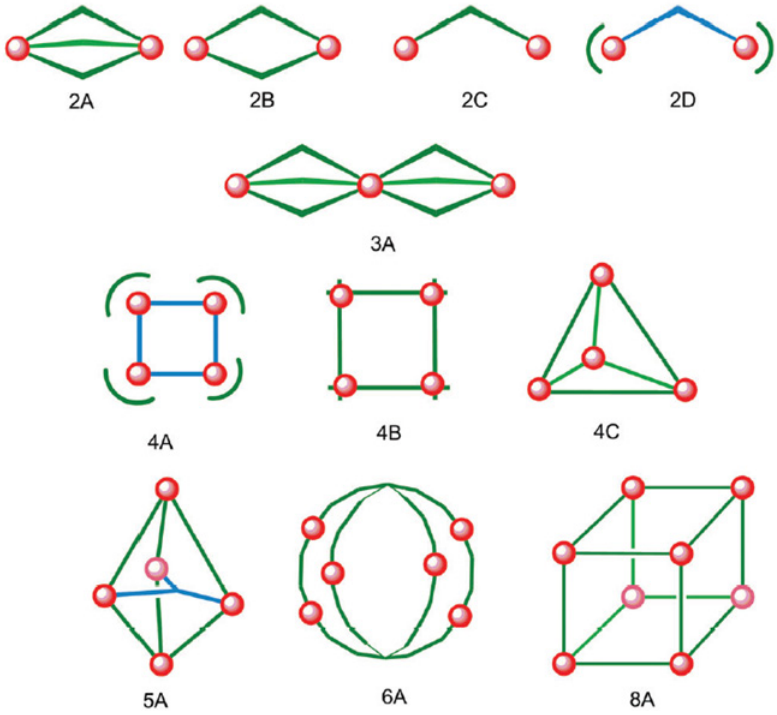

Scheme 1. Topologies observed for the discrete polynuclear Fe^{II} SCO complexes: binuclear (2A–2D), trinuclear (3A), tetranuclear, squares (4A), grids (4B), tetrahedral cages (4C), pentanuclear cage (5A), hexanuclear nanoball (6A) and octanuclear cube (8A). Green line represents bi- to polydentate nitrogen-donor ligand and blue line represents the bridging anion [7].

develop new ligand scaffolds to induce SCO behaviour in Fe^{II} tetranuclear cages and then to investigate the effects of various factors on SCO properties, including counter ions, substituents, solvent molecules as well as guest molecules. The second objective is to develop a potential application of these Fe^{II} SCO cages as colorimetric sensors for ammonia. The thesis was defended in public in October 2023 at UCLouvain, in the prestigious AGOR 12 auditorium, in front of a panel of several international and renowned scientists: Prof. Eric Gaigneaux (UCLouvain, Belgium and chair of the jury, a specialist in heterogeneous catalysis), Prof. Kamel Boukheddaden (Université Paris-Saclay, France, physicist, world specialist of SCO compounds), Prof. Bao-Lian Su (University of Namur, Belgium and University of Cambridge, UK), Prof. Michael Singleton (UCLouvain, Belgium, secretary of the jury, specialist in supramolecular chemistry), Dr. Koen Robeyns (UCLouvain, Belgium, crystallographer, ASM platform of IMCN institute) and Prof. Yann Garcia (UCLouvain, Belgium and vice-chair IBAME). The main research work includes several aspects which are developed below:

1. First SCO $Fe^{II}_4L_6$ cage based on pyridyl-hydrazone sites

To date, many reported Fe^{II} tetrahedral cages constructed from subcomponent self-assembly are LS, because pyridine-imine building blocks typically set up a strong ligand field [5]. However, an imidazole nitrogen atom usually exhibits a weaker ligand field strength than does a pyridine nitrogen atom, so imidazole-imine coordination units could have the necessary ligand field strength that leads to a SCO phenomenon. On this basis, Kruger [10], Nitschke [11], Gu [13, 15-17], Li [12], and Suzuki [18] used imidazole-imine coordination units to prepare several SCO tetrahedral cages. In 2019, Li and co-worker reported a SCO cage with thiazolyl-imine coordination sites, showing gradual temperature induced SCO behaviour with a 29 K hysteresis [14]. Thus, imidazole-imine and thiazolyl-imine sites were employed in all reported SCO cages, whereas the pyridyl-hydrazone combination has been rarely used. Pyridyl-hydrazone coordination mode in Fe^{II} SCO cage is not applied because of the ligand denticity. The ligand denticity of pyridyl-hydrazone based Fe^{II} SCO compounds is usually tridentate, which is actually not

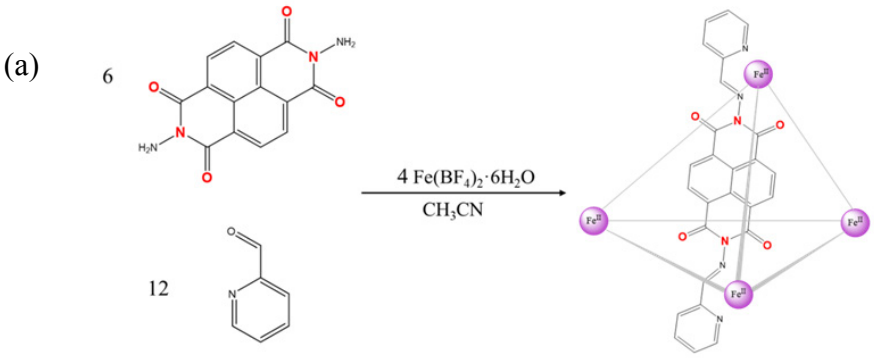

Figure 1. (a) Synthesis method of cage **1**. (b) Molecular structure of cage 1 in solid state at 120 K. The yellow lines connect four vertices of the Fe_4 tetrahedron. The given tetrahedron is either of ΔΔΔΔ or ΛΛΛΛ chirality at the Fe^{II} centers, with adjacent tetrahedra being of opposite chirality; C: dark grey; N: blue; Fe: orange; O: violet; H: white; B: pink; F: yellow [29].

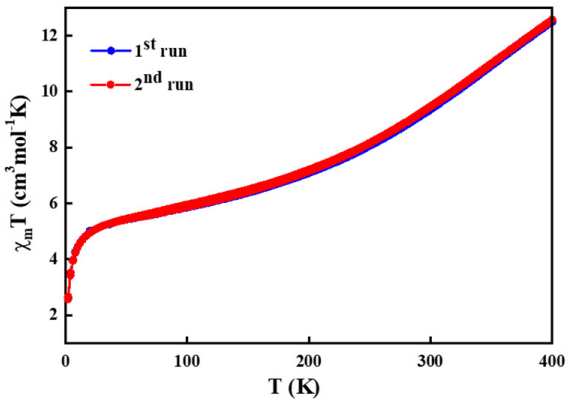

Figure 2. Temperature-dependent $\chi_m T$ plots for non-solvated cage **1**. The sample was annealed at 400 K in the SQUID cavity and two cycles of cooling and warming in the range 400–2 K were performed [29].

appropriate for the construction of Fe^{II} tetrahedral cages, which require tris-bidentate or bis-bidentate-type ligands to form $Fe^{II}{}_4L_4$ and $Fe^{II}{}_4L_6$ type cages, respectively [7]. In this section, we report the first SCO $Fe^{II}{}_4L_6$ (L = 2,7-bis(((*E*)-pyridin-2-ylmethylene) amino)benzo[lmn][3,8]phenanthroline-1,3,6,8(2*H*,7*H*)-tetraone) cage (**1**) synthesized through subcomponent self-assembly with pyridyl-hydrazone building block (**Figure 1a-1b**) [29].

Magnetic susceptibility measurements were performed over the range 400–2 K on non-solvated cage **1** (**Figure 2**), to avoid any apparent hysteresis loops associated to solvent removal [30]. At 400 K, $\chi_m T$ = 12.49 $cm^3 K\ mol^{-1}$, most likely originating from HS-Fe^{II} ions. However, traces of LS Fe^{II} ions may still be present, as the curve has not fully reached a plateau indicating incomplete SCO. Upon

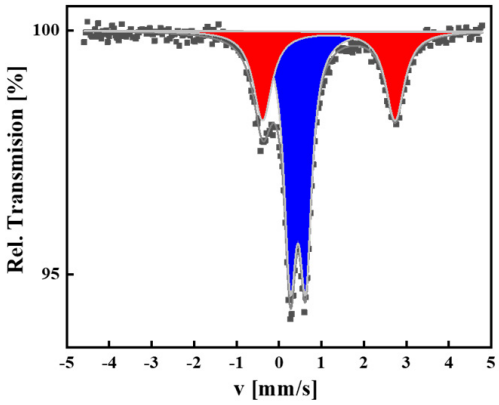

Figure 3. ^{57}Fe Mössbauer spectrum of non-solvated cage **1** recorded at 80 K. The red and blue quadrupole doublets correspond to HS and LS Fe^{II} ions, respectively [29].

cooling, the $\chi_m T$ value gradually decreases to 5.44 cm^3Kmol^{-1} at 50 K, presumably due to a SCO from HS to LS states of Fe^{II} ions. The sharp decrease in the $\chi_m T$ value below 25 K is likely due to zero-field splitting of the HS Fe^{II} ions [31]. Moreover, the curves of the first and second cycles overlap perfectly, indicating no hysteresis effect. Such gradual and incomplete SCO profile has also been observed in other polynuclear SCO complexes [12, 32].

The ^{57}Fe Mössbauer spectrum on non-solvated cage 1 recorded at 80 K exhibits two quadrupole doublets (**Figure 3**). A major one with an isomer shift of δ = 0.45 mm s^{-1} and a quadrupole splitting of ΔE_Q = 0.36 mm s^{-1}, characteristic of LS Fe^{II} ions, with an area fraction (A) of 62%. A second doublet [δ = 1.17 mm s^{-1}; ΔE_Q = 3.12 mm s^{-1}; A = 38%] corresponds to HS Fe^{II} ions. Thus, this spectrum supports the existence of Fe^{II} ions both in the LS and HS states, in agreement with the magnetic susceptibility analysis, further illustrating an incomplete SCO behaviour. Similar parameters have been identified in other polynuclear Fe^{II} complexes with a N_6 coordination core [11, 31] and no traces of oxidation to Fe^{III} were detected.

In conclusion, cage **1** represents the first Fe^{II} SCO cage with pyridyl-hydrazone ligand scaffolds, which is achieved by introducing additional carbonyl groups near the coordination site. These results suggest that reported LS molecular cages with pyridyl-imine sites could be reconsidered for SCO by carefully manipulating the functional groups in the ligand structure.

2. SCO in a family of $Fe^{II}_4L_6$ cages with pyridyl-hydrazone ligand scaffolds modulated by solvents, counter anions and substituents

In section 1, we have synthesized the first tetranuclear SCO Fe^{II} cage with pyridyl-hydrazone ligand scaffolds, replacing the ''classical'' imidazole-imine coordination units. However, the SCO profile for cage **1** is gradual, incomplete and without hysteresis loop, which limits the potential applicability. It is known from the literature that three factors including solvents, counter anions and substituents are crucial in determining the magnetic behavior of SCO materials [1-4]. In this section, we attempted for the first time to study the anion and substituents effects on SCO behaviour in this cage family on the basis of cage **1**. Five new Fe^{II} tetrahedral cages were synthesized through subcomponent self-assembly using the same pyridine-hydrazone ligand scaffold but with different anions ClO_4^- (**2**), $CF_3SO_3^-$ (triflate, OTf^-, **3**) and $C_2F_6S_2O_4N^-$ (triflimide, NTf_2^-, **4**) and different substituents R on the pyridine ring (R = CH_3, **5**; R = OCH_3, **6**) (**Scheme 2**). Cage **2-6** have been structurally confirmed by single crystal X-ray diffraction (except **4**) and electrospray ionization time-of-flight mass spectrometry. The magnetic properties were carefully investigated by SQUID magnetometry and ^{57}Fe Mössbauer spectroscopy.

To investigate the solvents effects on the SCO profile of cage **2**, dc magnetic susceptibility experiments were performed on **2** and *in situ* obtained **2**•desolvated

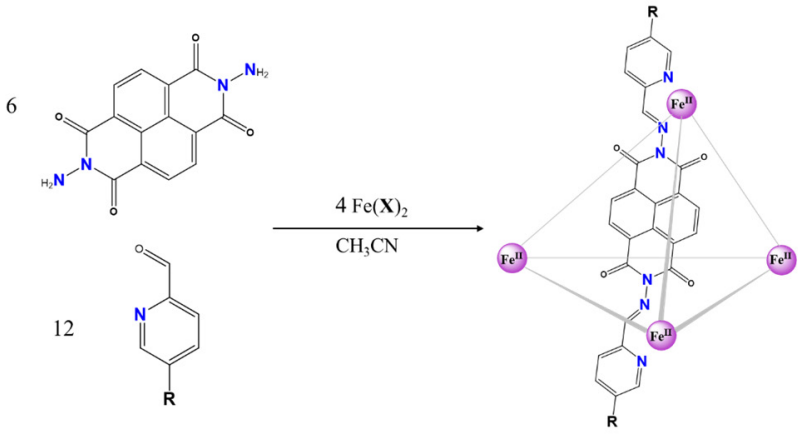

Cage **1**: R = H; X = BF_4^- Cage **2**: R = H; X = ClO_4^-
Cage **3**: R = H; X = OTf^- Cage **4**: R = H; X = NTf_2^-
Cage **5**: R = CH_3; X = ClO_4^-
Cage **6**: R = OCH_3; X = ClO_4^-

Scheme 2. Schematic representation of the Fe^{II} complex structures studied in this section [33].

in the solid state at different temperature ranges. The molecular formula of cage **2** was confirmed by elemental analysis and TGA as $Fe^{II}_4L_6(ClO_4)_8$•$10H_2O$. As shown in black curve of **Figure 4**, the χ_mT value of cage **2** gradually decreases from 5.24 cm^3•mol^{-1}•K at 300 K to 2.27 cm^3•mol^{-1}•K at 50 K, indicating that approximately one Fe^{II} center has undergone a spin state transition from HS to LS, as the expected spin-only χ_mT value of the one HS Fe^{II} ion is 3 cm^3•mol^{-1}•K [9, 11]. The subsequent heating curve from 2 to 300 K overlaps well with the cooling curve, demonstrating that the SCO behavior is reversible and without hysteresis. After annealing at 400 K, non-solvated compound $Fe^{II}_4L_6(ClO_4)_8$ (**2**•desolvated) was obtained. The χ_mT value at 400 K is 11.05 cm^3•mol^{-1}•K, however the shape of the curve shows that the cage is not in the fully HS state. As the temperature is lowered, the χ_mT product again gradually decreases, with a trend similar to that of **2**. At 50 K, the χ_mT product is 3.42 cm^3•mol^{-1}•K, suggesting that one Fe^{II} center remained in the HS state, *i.e.* [1HS-3LS], while about two Fe^{II} centers experienced SCO during the cooling process. The slight decrease in χ_mT below 20 K for both samples is likely attributed to zero-field splitting of the HS Fe^{II} ions [31]. Similarly, no hysteresis effect was observed in the profile. Thus, the presence of solvent molecules appears to stabilize the LS state, as indicated by the lower χ_mT values at the same temperature compared to **2**•desolvated, but without a huge effect on the SCO profile

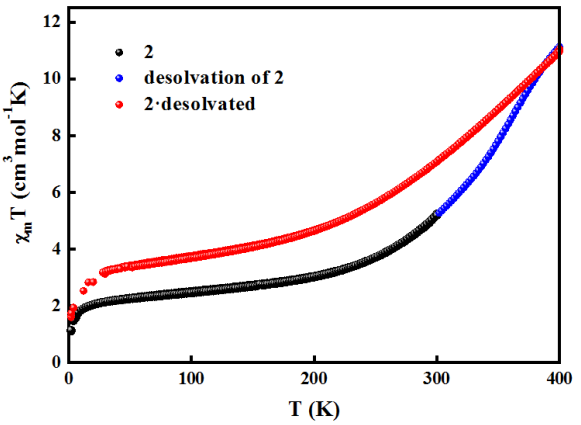

Figure 4. Temperature dependence of the χ_mT product for cage **2** (black circles; 300-2-400 K), desolvation of **2** in the SQUID chamber (blue circles; 302-400 K) and desolvated cage **2** (red circles; two cooling and heating cycles in the range of 400-2 K) [33].

such as the transition temperature as well as the very gradual transition behaviour. This phenomenon is presumably attributed to the guest effect in SCO supramolecular cage compounds, in which water molecules form weak interactions such as hydrogen bonds with N (pyridyl-hydrazone groups) or O (ketone groups) atoms in the ligand system near the Fe^{II} centers, thus changing the electronic environment around the Fe^{II} nucleus and affecting its spin state [13, 34]. Previous studies performed on analogous SCO Fe^{II} cage compounds demonstrated a similar trend [10, 13] .

To single out the effect of counterions on the magnetic properties of the tetranuclear cage family, cage **1-4** were synthesized with different counter anions (BF_4^-, ClO_4^-, OTf^- and NTf_2^-, respectively) while all solvent molecules were removed in the SQUID cavity. As shown by the green curve of **Figure 5**, the χ_mT value for **3** is 12.40 cm^3•mol^{-1}•K at 400 K, decreasing to 6.03 cm^3•mol^{-1}•K at 50 K as the temperature decreases, presumably due to a SCO from HS to LS states of Fe^{II} ions. In addition, the χ_mT product at 50 K indicates approximately two Fe^{II} centers are presented in the LS states, *i.e.* [2HS-2LS], similar to cage **1** but with one more HS center than cage **2**. The decrease in χ_mT below 20 K is ascribed to zero-field splitting of the HS Fe^{II} ions [31]. Hysteresis phenomenon was also not observed during the two rounds of heating and cooling processes in cage **3**. The magnetic susceptibility experiment for cage **4** is in progress at the collaborating partner. Thus, from the available magnetic data it is evident that the counter anions influence the spin state of the Fe^{II} ions, *e.g.* at 80 K the spin states of cages **1**, **2**, **3** are [2HS-2LS], [1HS-3LS] and [2HS-2LS] respectively. However, the effect on the SCO behaviour is not significant, *i.e.* cages **1**, **2** and **3** all possess incomplete, gradual and non-hysteresis SCO characteristics. Furthermore, we noticed that the anion change did not effectively enhance the cooperativity in the system leading to no significant modification in the SCO profiles. This may be due to the fact that the anions are not located in the internal cavities of **1-3** and therefore the host-guest interaction is weak, not sufficient to cause any structural changes (Fe-N bond

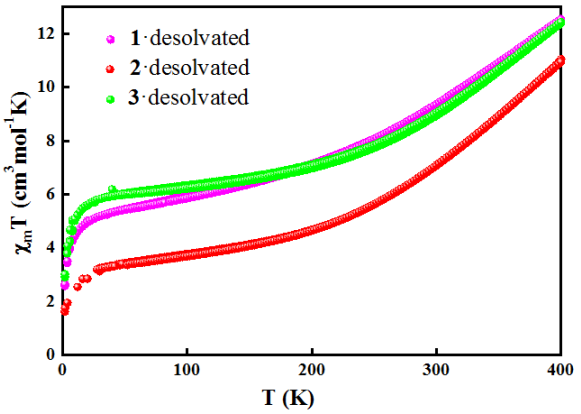

Figure 5. Temperature dependence of the $\chi_m T$ product for desolvated cage **1-3** in the range 400–2 K (two cycles of cooling and warming) [33].

length) or alter the geometry of the metal ion in the cages during the spin transition [35, 36]. Also, the volume of the counter anions is not directly related to the distribution of the spin states, as the volumes of BF_4^- (53 Å^3) and OTf^- (85 Å^3) differ significantly [37], but the spin states of the Fe^{II} ions are analogous, unlike the pattern observed in the $[Fe(4\text{-amino-}1,2,4\text{-triazole})3]^{2+}$ 1D polymer chain and tetranuclear grid systems. The magnetic susceptibility measurements for **5** and **6** are in progress, so the effect of the substituent on the SCO is not discussed.

The ^{57}Fe Mössbauer spectrum on the non-solvated cage **2** recorded at 80 K shows two quadrupole doublets (**Figure 6b**). The first doublet with blue color exhibits an isomer shift of δ = 0.45 mm s^{-1} and a quadrupole splitting ΔE_Q = 0.35 mm s^{-1}, corresponding to typical LS Fe^{II} ions, with an area fraction (A) of 80%. The second doublet with red color [δ = 1.19 mm s^{-1}; ΔE_Q = 3.09 mm s^{-1}; A = 20%] is assigned to HS Fe^{II} ions. Similar Mössbauer spectrum parameters can be identified in other previously reported polynuclear Fe^{II} complexes with a FeN_6 coordination mode [29, 31]. The spectrum therefore demonstrates the presence of Fe^{II} ions in the LS and HS states and in a ratio of approximately 3:1, in agreement with the results of the magnetic susceptibility analysis, further illustrating an incomplete SCO behaviour. The Mössbauer spectrum of **3**•desolvated also exhibits two quadrupole doublets: [δ = 0.44 mm s^{-1}; ΔE_Q = 0.35 mm s^{-1}; A = 56%; blue] and [δ = 1.17 mm s^{-1}; ΔE_Q = 3.13 mm s^{-1}; A = 44%; red], corresponding to LS and HS Fe^{II} ions, respectively (**Figure 6c**). The LS/HS Fe^{II} ratio is 56 : 44%, similar to that of **1** at 80 K [62% (δ = 0.45 mm s^{-1}; ΔE_Q = 0.36 mm s^{-1}) : 38% (δ = 1.17 mm s^{-1}; ΔE_Q = 3.12 mm s^{-1})] (**Figure 6a**), which is close to [2HS-2LS] spin states pattern and is consistent with the magnetic susceptibility analysis. ^{57}Fe Mössbauer data for cage **4-6** are in progress.

Thus, in this section, we have successfully synthesized five new Fe^{II} tetrahedral cages using the same pyridine-hydrazone ligand scaffold but with different anions as well as substituents (**2-6**) to study the solvents, counterions and substituents effects on SCO properties. The solvent effects on SCO were studied in cage **2**. Temperature-dependent $\chi_m T$ plots show that the presence of solvent molecules seems to stabilize the LS state but does not have a dramatic effect on the SCO profile. The anions effects were studied among the desolvated cages **1-3**. The magnetic data show that the counter-anions influence the spin state distributions of the Fe^{II} ions.

(To be continued . . .)

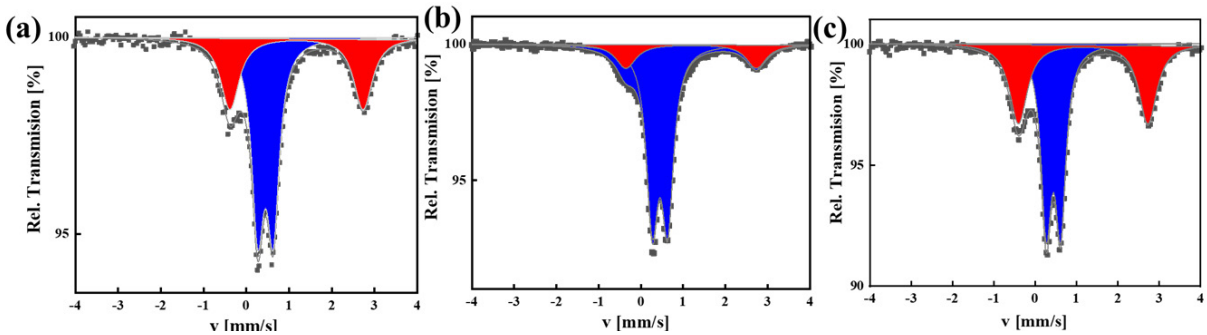

Figure 6. ^{57}Fe Mössbauer spectrum of desolvated samples of cage **1** (a), cage **2** (b) and cage **3** (b) recorded at 80 K. The blue and red quadrupole doublets corresponding to LS and HS Fe^{II} ions, respectively [33].

Future Conferences, Symposia, Workshops

August 14- 16, 2025
16th National Conference on Mössbauer Spectroscopy
Dalian, China
https://wangjh.dicp.ac.cn/info/1090/3142.htm (Chinese)
https://wangjh.dicp.ac.cn/info/1119/3143.htm (English)

September 7 - 12, 2025
ICAME & HYPERFINE 2025 38th International Conference on the Applications of the Mössbauer Effect, ICAME, and the International Conference on Hyperfine Interactions and Their Applications, HYPERFINE
Gdańsk, Poland
https://icame-hi-2025.pollub.pl/

Center for Advanced Mössbauer Spectroscopy

Dalian Institute of Chemical Physics, Chinese Academy of Sciences

is pleased to offer these services of the Mössbauer spectra (MS) measurement & analysis to the international community. Your any special request will be carefully considered.

We offer

- Room temperature ^{57}Fe/ ^{119}Sn MS
- Room temperature ^{57}Fe / ^{119}Sn CEMS
- Low temperature transmission ^{57}Fe MS
- Frozen solution ^{57}Fe MS
- Electrochemical in-situ/operando ^{57}Fe / ^{119}Sn MS
- Ion battery in-situ/operando ^{57}Fe / ^{119}Sn MS
- Photocatalytic in-situ/operando ^{119}Sn MS
- Photoelectrocatalytic in-situ/operando ^{57}Fe / ^{119}Sn MS
- Temperature, pressure and atmosphere control in-situ/operando ^{57}Fe / ^{119}Sn MS

Contact

Email: mossbauer@dicp.ac.cn

Phone: +86-411-84379711

Center for Advanced Mössbauer Spectroscopy
Dalian Institute of Chemical Physics
Chinese Academy of Sciences
457 Zhongshan Road, Dalian 116023, China

http://wangjh.dicp.ac.cn/csfw.htm
http://wangjh.dicp.ac.cn/English/Services.htm

RITVERC
Isotopenprodukte

#Co-57
#Sn-119m
#Fe-57 reference absorbers
#Source grippers

Since 2023 → a new distributor in North and South America:
ISOFLEX Radioactive LLC, iso-rad.com, +1 (415) 440-4433

ritverc.com